
Adversarial Audio Synthesis with Complex-valued Polynomial Networks

Yongtao Wu

KTH Royal Institute of Technology
yongtaowu98@gmail.com

Grigorios G Chrysos

EPFL, Switzerland
grigorios.chrysos@epfl.ch

Volkan Cevher

EPFL, Switzerland
volkan.cevher@epfl.ch

Abstract

Time-frequency (TF) representations in audio synthesis have been increasingly modeled with real-valued networks. However, overlooking the complex-valued nature of TF representations can result in suboptimal performance and require additional modules (e.g., for modeling the phase). To this end, we introduce complex-valued polynomial networks, called APOLLO, that integrate such complex-valued representations in a natural way. Concretely, APOLLO captures high-order correlations of the input elements using high-order tensors as scaling parameters. By leveraging standard tensor decompositions, we derive different architectures and enable modeling richer correlations. We outline such architectures and showcase their performance in audio generation across four benchmarks. As a highlight, APOLLO results in 17.5% improvement over adversarial methods and 8.2% over the state-of-the-art diffusion models on SC09 dataset in audio generation. Our models can encourage the systematic design of other efficient architectures on the complex field.

1 Introduction

Generative Adversarial Networks (GANs) enable photo-realistic synthesis in image-related tasks [17, 29, 33, 3, 7]. Their stellar performance has prompted their use in unconditional audio synthesis, which aims to synthesize consistent utterances from noise [11, 13, 41, 47]. However, the human perception is sensitive to both global and local coherence of the waveform [13], which makes audio synthesis an inherently challenging task. We argue that the design choices, i.e., the audio representations and the network architecture, hold a key role in successful audio synthesis.

Raw waveform is primarily used for unconditional speech generation [11]. Recent studies focus on the two-dimensional time-frequency (TF) representation due to its both increased performance and the theoretical expressivity [10, 48, 41]. In the TF representation, the raw waveform is transformed through the Short-time Fourier transform (STFT) or Constant-Q transform (CQT) to the frequency domain, which is naturally expressed with complex numbers. To avoid using complex numbers often the phase information is discarded and only the magnitude is maintained. However, dropping the phase deteriorates the performance and results in a lack of phase coherence in synthesized audio [13]. Importantly, without the phase information, the TF representation is not invertible. This raises the question: *How can we explicitly model the complex-valued TF representation?*

A complex number can be expressed using two real numbers, so a real-valued neural network (RVNN), i.e., a typical feed-forward neural network, with two real-valued outputs could represent complex numbers. The TF representation can then be thought of as a two-channel image, which enables

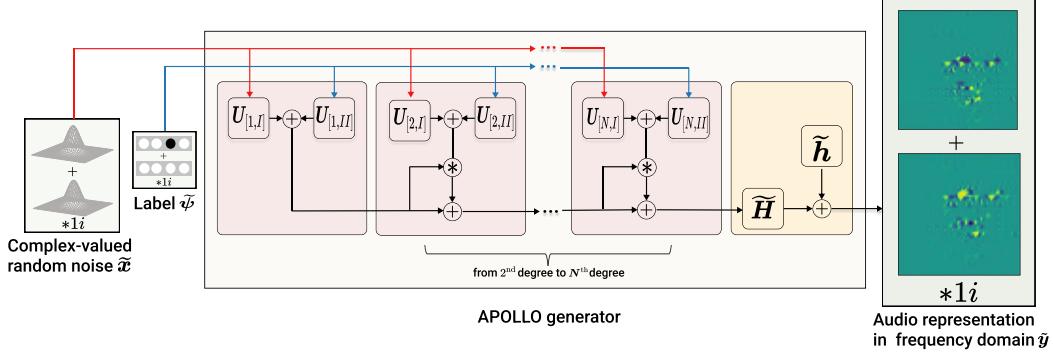


Figure 1: In this work we propose a class of functions, called APOLLO, where the complex-valued output is a polynomial of the complex-valued input. The input of the APOLLO generator is complex-valued noise and the output is the representation of audio in the frequency domain (e.g., STFT, CQT). APOLLO can also receive conditional information, e.g., class-label, which can be treated as a complex-valued one-hot vector with zero imaginary part. The generator in the schematic corresponds to (6). All learnable parameters inside pink blocks (yellow blocks) are real-valued (complex-valued).

us to utilize the progress made on RVNNs in the previous decade [25]. However, a more natural representation is to design complex-valued neural networks (CVNNs) with complex-valued weights or complex-valued inputs/outputs. Incidentally, CVNNs have demonstrated higher generalization ability [27], which is partly attributed to the degree of freedom at the synaptic weighting of two-channel RVNNs being increased due to complex multiplication [2]. Even though the richer capacity has led to an increasing attention on CVNNs [62, 4, 72], CVNNs have yet to demonstrate state-of-the-art performance on audio generation.

On the other hand, recent theoretical advances [31, 14] prove that models with second-degree polynomials enlarge the set of functions that can be represented exactly with zero error. Polynomial nets have demonstrated flexibility and efficiency over standard neural networks in various tasks, e.g., image generation [33, 7], image recognition [68], reinforcement learning [31], and sequence modelings [59]. This motivates us to design a class of polynomial nets, called APOLLO, that extracts complex-valued representations for audio generation. We utilize complex-valued polynomial networks that express a complex-valued output as a high-degree polynomial expansion of the complex-valued input, as illustrated in Fig. 1. The unknown parameters of the expansion are naturally represented as tensors, and we use standard tensor decompositions for reducing the number of learnable parameters. We determine how specific decompositions result in simple recursive formulations that enable us to implement arbitrary degree polynomial expansions efficiently. We conduct a number of experiments that exhibit the efficacy of APOLLO in unconditional (conditional) audio generation and multimodal generation. Overall, our contributions can be summarized as follows:

- We introduce a new class of complex-valued polynomial neural networks. We reveal how different architectures can be obtained by changing the factorization of the unknown parameters in the polynomial expansion.
- We conduct a thorough evaluation on audio generation and showcase the advantage of APOLLO when compared with the prior art. Through directly modelling the complex-valued TF representation, APOLLO is free of phase estimation.
- APOLLO is extended in case of multiple inputs, e.g., when additional variables are available. We implement such a polynomial expansion on conditional audio generation. Additionally, we investigate the efficacy of learning shared representations on multimodal generation.
- Lastly, our model can also be applied in additional audio-related tasks, e.g., speech recognition and speech enhancement.

We believe that our results can further encourage the research community to consider the complex representations, especially in the context of polynomial networks. Therefore, we will make the source code available upon the acceptance of the paper to accelerate such experimentation.

2 Related work

Audio generation. Unconditional audio generation aims to generate audio creatively, which has practical significance in the real world [41, 11, 13, 47]. WaveGAN and SpecGAN [11] are the first attempts to unconditionally synthesize audio using GANs. WaveGAN directly models the raw audio while SpecGAN models the log spectrum of the STFT in the frequency domain. The drawback of SpecGAN includes the demand for phase recovery with Griffin-Lim [18] during synthesis step. GANSynth [13] improves the previous work by jointly modeling the mel-spectrogram and the instantaneous frequency, which results in more consistent harmonics and avoids additional phase estimation technique. However, the phase misalignment in GANSynth leads to energy loss due to the cancellation of frequency bands [41]. Similar to SpecGAN, TiFGAN [41] only models the log spectrum of the STFT while it estimates the phase by Phase-gradient heap integration (PGHI) [49], which avoids expensive iterative Griffin-Lim in SpecGAN and magnitude integration in GANSynth. Gunasekaran et al. [21] improve the conditional spoken digit generation using mel-spectrogram and Griffin-Lim. Haque et al. [23] propose GGAN to achieve high fidelity audio generation with a fewer labelled audio clips, which rely on log spectrum representation and PGHI recovery. Contrary to most aforementioned methods, our APOLLO directly models the STFT in the complex domain without using phase recovery. Apart from adversarial generation, diffusion-based models (DiffWave [37]) and state space [19] based models (SASHIMI [16]) are also receiving increasing attention. Compared with adversarial methods, DiffWave results in slower inference speed due to the reverse process. Lastly, text-to-speech (TTS) systems, as another category of audio generation, generate the audio representation based on the text information and then utilize a neural vocoder to obtain the waveform. Many solutions are proposed in recent years [66, 32, 69, 57, 65]. Both SASHIMI and DiffWave can also be implemented as neural vocoder and achieve excellent performance against WaveNet [66].

Complex-valued neural networks (CVNNs). The ideas behind CVNNs can be traced back to at least Kim and Guest [34] that derive backpropagation rules with respect to a real and an imaginary part. The mathematical motivation as well as the biological feasibility of CVNNs has been explored during the previous decade [51, 64]. Being equipped with a rich representational capacity in the complex field, CVNNs have drawn increasing attention in a wide range of applications. Oyallon and Mallat [46] design a deep scattering convolution network to improve the performance of image descriptors. Trouillon et al. [63] use complex-valued embeddings for simple link prediction. In audio-related tasks, the noise speech is enhanced by being converted and passed through STFT, complex-valued network, and inverse STFT [4]. Another line of research applies complex operations on top of typical neural networks. Arjovsky et al. [1] use complex operations on recurrent neural network to circumvent problems of vanishing and exploding gradients. Trabelsi et al. [62] propose complex convolutional networks and algorithms for complex batch-normalization, complex weight initialization, and complex activations.

Polynomial neural networks (PNNs). PNNs have been studied for several decades [30, 15, 58, 44, 39, 71]. However, many of the aforementioned PNNs do not scale well for high-dimensional data samples, such as those required for modern generative models. Chrysos et al. [6] introduce a high-degree polynomial generator, which approximates the distribution of high-dimensional data. The work was subsequently extended on a range of applications in the class of function approximators called Π -Nets, where Chrysos et al. [9] exhibit the increased expressivity of real-valued PNNs. Lastly, Zhang et al. [73] focus on approximating the operations such as sigmoid, ReLU, and max pooling with polynomial operations. Differently from previous works, we explicitly propose polynomial expansions on the complex field.

3 Methods

Notation We introduce the core operators/symbols, while a more detailed notation is deferred to Sec.A in the appendix. Real-valued vectors/matrices/tensors are symbolized by lower-case/uppercase/calligraphic boldface letters, e.g., \mathbf{y} , \mathbf{Y} , \mathcal{Y} . All complex-valued variables are symbolized with wide tilde, e.g., $\tilde{\mathbf{y}}$, $\tilde{\mathbf{Y}}$, $\tilde{\mathcal{Y}}$. The mode- m vector product between a complex-valued tensor and multiple complex-valued vectors is denoted as: $\tilde{\mathcal{Y}} \times_1 \tilde{\mathbf{u}}^{(1)} \times_2 \tilde{\mathbf{u}}^{(2)} \times_3 \cdots \times_M \tilde{\mathbf{u}}^{(M)} = \tilde{\mathcal{Y}} \prod_{m=1}^M \times_m \tilde{\mathbf{u}}^{(m)}$. Khatri-Rao product and Hadamard product are denoted by \odot and $*$, respectively.

3.1 Complex Polynomial Neural Networks

According to Mergelyan’s Theorem [55], any smooth complex-valued function could be approximated by a polynomial. A complex polynomial refers to a polynomial expansion with complex-valued coefficients. Our goal is to learn an N^{th} degree polynomial expansion with respect to the input $\tilde{\mathbf{x}} \in \mathbb{C}^d$ with an o -dimensional output $\tilde{\mathbf{y}}$ as follows:

$$\tilde{\mathbf{y}} = \sum_{n=1}^N \left(\tilde{\mathcal{W}}^{[n]} \prod_{j=2}^{n+1} \times_j \tilde{\mathbf{x}} \right) + \tilde{\mathbf{h}}, \quad (1)$$

where $\left\{ \tilde{\mathcal{W}}^{[n]} \in \mathbb{C}^{o \times \prod_{m=1}^n \times_m d} \right\}_{n=1}^N$ and $\tilde{\mathbf{h}} \in \mathbb{C}^o$ are learnable parameters. The drawback of (1) is that it requires an exponential number of parameters for high-degree polynomial expansions, which is not scalable. Instead, we will apply coupled CP decomposition with factor sharing to reduce the learnable parameters [36, 9]. Firstly, we introduce polynomial expansions with complex-valued input variables and complex-valued coefficients, where the real and the imaginary coefficients are modelled with independent variables. Sequentially, we make additional assumptions that can further reduce the parameters and lead to efficient implementations. We illustrate below the derivation of CFC for third-degree expansion, while we stress out that the recursive formulation can be applied for *any arbitrary degree polynomial expansion*.

CFC (Fully coupled decomposition) In the first model we assume all the weight tensors $\{\tilde{\mathcal{W}}^{[n]}\}_{n=1}^N$ of (1) are jointly factorized by a coupled CP decomposition to share factors between different degrees. For a third-degree expansion that becomes:

- First degree parameters: $\tilde{\mathcal{W}}^{[1]} = \tilde{\mathbf{H}} \tilde{\mathbf{U}}_{[1]}^T$.
- Second degree parameters: $\tilde{\mathcal{W}}_{(1)}^{[2]} = \tilde{\mathbf{H}} (\tilde{\mathbf{U}}_{[3]} \odot \tilde{\mathbf{U}}_{[1]})^T + \tilde{\mathbf{H}} (\tilde{\mathbf{U}}_{[2]} \odot \tilde{\mathbf{U}}_{[1]})^T$.
- Third degree parameters: $\tilde{\mathcal{W}}_{(1)}^{[3]} = \tilde{\mathbf{H}} (\tilde{\mathbf{U}}_{[3]} \odot \tilde{\mathbf{U}}_{[2]} \odot \tilde{\mathbf{U}}_{[1]})^T$.

By leveraging the aforementioned factorization and utilizing simple algebra, a simple recursive form can be retained (which is also generalizable to an N^{th} degree polynomial) as we prove in Sec.C.1:

$$\tilde{\mathbf{y}}_n = \left(\tilde{\mathbf{U}}_{[n]}^T \tilde{\mathbf{x}} \right) * \tilde{\mathbf{y}}_{n-1} + \tilde{\mathbf{y}}_{n-1}, \quad (2)$$

for $n = 2, \dots, N$ with $\tilde{\mathbf{y}}_1 = \tilde{\mathbf{U}}_{[1]}^T \tilde{\mathbf{x}}$ and $\tilde{\mathbf{y}} = \tilde{\mathbf{H}} \tilde{\mathbf{y}}_N + \tilde{\mathbf{h}}$, where $\tilde{\mathbf{U}}_{[n]} \in \mathbb{C}^{d \times k}$, $\tilde{\mathbf{H}} \in \mathbb{C}^{o \times k}$, $\tilde{\mathbf{h}} \in \mathbb{C}^o$. Intuitively, each recursive term increases the degree of expansion by one, using three fundamental operations: a) an affine transformation with the input, i.e., $\tilde{\mathbf{U}}_{[n]}^T \tilde{\mathbf{x}}$, b) an element-wise product with the previous term, c) a skip connection with the previous term. Those three operations are easy to implement and enable any arbitrary degree of expansion to be achieved.

CFBC (Fully coupled decomposition with bias) In this section, we develop a new decomposition to allow the existence of bias term $\tilde{\rho}_{[n]} \in \mathbb{C}^k$ compared with the previous model, which can increase the expressivity of model in practice. The recursive relation is as follows (proof in Sec.C.2)

$$\tilde{\mathbf{y}}_n = (\tilde{\mathbf{U}}_{[n]}^T \tilde{\mathbf{x}} + \tilde{\rho}_{[n]}) * \tilde{\mathbf{y}}_{n-1}, \quad (3)$$

for $n = 2, \dots, N$ with $\tilde{\mathbf{y}}_1 = \tilde{\mathbf{U}}_{[1]}^T \tilde{\mathbf{x}}$ and $\tilde{\mathbf{y}} = \tilde{\mathbf{H}} \tilde{\mathbf{y}}_N + \tilde{\mathbf{h}}$.

CBC (Coupled decomposition with bias) The model above assumes different parameters for the real and the imaginary part, however, we could also perform sharing of certain factors between the real and the imaginary part to reduce the learnable parameters. Even though multiple sharing of factors could be implemented, we have assumed that every factor is shared apart from the factor corresponding to the unfolding dimension. That is, all terms between the real and the imaginary coefficients are shared apart from the matrix $\tilde{\mathbf{H}}$. The following recursive relationship between different degrees is obtained: (proved in Sec.C.3):

$$\tilde{\mathbf{y}}_n = (\mathbf{U}_{[n]}^T \tilde{\mathbf{x}} + \rho_{[n]}) * \tilde{\mathbf{y}}_{n-1}, \quad (4)$$

for $n = 2, \dots, N$ with $\tilde{\mathbf{y}}_1 = \mathbf{U}_{[1]}^T \tilde{\mathbf{x}}$ and $\tilde{\mathbf{y}} = \tilde{\mathbf{H}} \tilde{\mathbf{y}}_N + \tilde{\mathbf{h}}$. Compared with the recursive formulation (3) in the previous decomposition, we observe that (4) reduces the number of parameters by converting $\tilde{\mathbf{U}}_{[n]} \in \mathbb{C}^{d \times k}$ to $\mathbf{U}_{[n]} \in \mathbb{R}^{d \times k}$ and $\tilde{\rho}_{[n]} \in \mathbb{C}^k$ to $\rho_{[n]} \in \mathbb{R}^k$ among each degree.

3.2 Other model variants

To obtain more expressive models, we can further apply a joint hierarchical decomposition instead of separating the interactions between different degrees or add a shortcut connection embedded into the relationship, which is motivated by the skip connections in ResNet [25]. In addition, the aforementioned models assume polynomial with complex-valued coefficients. However, we can also simplify the models and implement them with real-valued coefficients, i.e., we could replace $\tilde{\mathbf{H}}$ with real-valued matrix \mathbf{H} , $\tilde{\mathbf{h}}$ with real-valued vector \mathbf{h} . Due to the lack of space, we defer these models to the appendix (Sec.B) for completion.

3.3 Conditional complex-valued polynomial

The aforementioned polynomial expansions rely on a single input variable, however often there are additional variables available, e.g., class-label information. In this case, we can design polynomial expansions from multiple input variables. Motivated by the real-valued multivariate analysis [7], we focus on the case of two complex-valued inputs $\tilde{\mathbf{x}} \in \mathbb{C}^d$ and $\tilde{\boldsymbol{\psi}} \in \mathbb{C}^d$, but the expansions can be trivially extended to arbitrary number of inputs and also support different dimensions for the inputs. Unlike (1), our goal turns to learn an N^{th} degree polynomial expansion with an o -dimensional output $\tilde{\mathbf{y}}$ with two inputs:

$$\tilde{\mathbf{y}} = \sum_{n=1}^N \sum_{\gamma=1}^{n+1} \left(\tilde{\mathbf{w}}^{[n,\gamma]} \prod_{j=2}^{\gamma} \times_j \tilde{\mathbf{x}} \prod_{\tau=\gamma+1}^{n+1} \times_{\tau} \tilde{\boldsymbol{\psi}} \right) + \tilde{\mathbf{h}} \quad (5)$$

Similar to the single-variable polynomial, (5) could be expressed to the following recursive relationship by applying coupled CP decomposition:

$$\tilde{\mathbf{y}}_n = \left(\mathbf{U}_{[n,I]}^T \tilde{\mathbf{x}} + \mathbf{U}_{[n,II]}^T \tilde{\boldsymbol{\psi}} \right) * \tilde{\mathbf{y}}_{n-1} + \tilde{\mathbf{y}}_{n-1} \quad (6)$$

for $n = 2, \dots, N$ with $\tilde{\mathbf{y}}_1 = \mathbf{U}_{[1,I]}^T \tilde{\mathbf{x}} + \mathbf{U}_{[1,II]}^T \tilde{\boldsymbol{\psi}}$ and $\tilde{\mathbf{y}} = \tilde{\mathbf{H}} \tilde{\mathbf{y}}_N + \tilde{\mathbf{h}}$, where $\mathbf{U}_{[n,I]} \in \mathbb{R}^{d \times k}$, $\mathbf{U}_{[n,II]} \in \mathbb{R}^{d \times k}$. Note that other decompositions discussed in Sec.B can also be used.

3.4 Adversarial audio generation

In the majority of our experimental validation we use GANs, where APOLLO is chosen as the generator while the discriminator is a standard ResNet. Wasserstein loss with gradient penalty is used as the criterion of GAN due to its stability and robustness [20]. On unconditional audio generation, we implement the generator using single-variable models, e.g., the models in Sec.3.1, 3.2. The generator receives a complex-valued noise and outputs the representation of audio in the frequency domain, as illustrated in Fig.6. Given an audio clip, we apply STFT and truncate the Nyquist bin to obtain the complex-valued representation. As visually depicted in Fig.2, the imbalanced distribution of the raw real part and the imaginary part of STFT is not well-suited for the Tanh activation of the generator. We introduce a series of pre-processing steps for training. Specifically, we first divide the real part and the imaginary part by its maximum value to limit the range between [-1,1] in order to match the output distribution of tanh activation function in the generator. In view of previous work that model the spectrum in log-scale, we take the square root of the absolute value of the real part (the imaginary part) and keep its sign. This technique is denoted as 'SQRT' in Fig.2. Lastly, unless mentioned otherwise, we assume that ReLU activation are inserted after each degree, which result in a piece-wise polynomial expansion and tanh activation after the final degree.

When class label is available, we can also use a class-conditional generator, in which case we choose the two-input polynomial expansion. Given a noise vector $\tilde{\mathbf{x}} \in \mathbb{C}^{d_1}$ and one-hot label vector $\tilde{\boldsymbol{\psi}} \in \mathbb{C}^{d_2}$ with zero imaginary part, the generator can be implemented based on (6), as shown in Fig.1.

Previous methods focus exclusively on a single modality, i.e., audio. However, as humans we perceive information using varying sources from the real-world. To this end, we extend our APOLLO to multimodal generation (from image to audio). A schematic of the generator is visually depicted in Fig.3. Specifically, we first use two low-degree APOLLOs for the random noise and the image, respectively. A high-degree conditional APOLLO, proposed in Sec.3.3, is utilized to capture the correlations between the outputs of these two low-degree APOLLOs and generate the complex-valued representation, e.g., STFT and CQT of the audio.

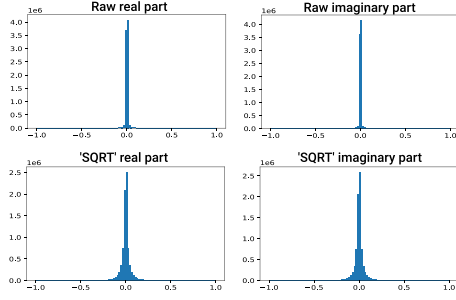


Figure 2: **Top:** The raw distribution of the real part and the imaginary part of STFT. **Bottom:** The distributions of the real part and the imaginary part of STFT with pre-processing techniques 'SQRT' become more even.

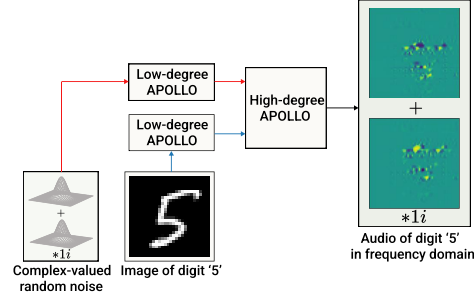


Figure 3: Generator used in image-to-speech experiments. A two-variable, high-degree APOLLO is utilized to capture the correlations of the two input variables.

Difference from II-Nets: APOLLO differs substantially from II-Nets in: a) The new decompositions that yield (3) and (4) are designed for reducing the number of parameters when extending to complex field and increasing the expressivity with the new bias term. b) We design architectures and technique for audio generation in Sec.3.4 while II-Nets is mostly focused on image-related tasks. c) II-Nets have been used for a single variable input, while we also demonstrate experiments with two variables. e.g., conditional generation and multi-modal generation. Further discussion can be found in Sec.B.3.

4 Experiments

We first conduct a series of experiments on audio generation to evaluate our framework. Then we further analyze the trained models. Lastly, we extend our model to additional audio-related tasks.

4.1 Comparison against adversarial-based models in audio generation

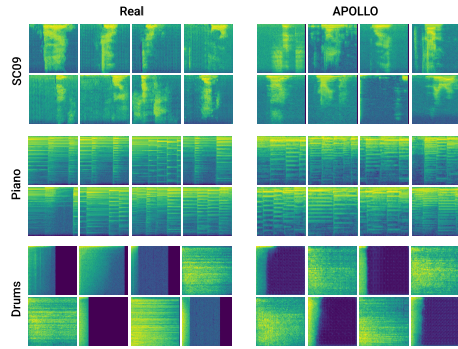
4.1.1 Unconditional audio generation

Our first experiment evaluates APOLLO on unconditional audio generation, where the generator receives complex-valued noise and outputs the TF representation of audio, as illustrated in Fig.6 (appendix). We conduct experiments on three datasets used in Donahue et al. [11]: (a) Speech Commands Zero Through Nine (SC09). (b) Piano dataset. (c) Drum dataset. Further details on the dataset, evaluation metrics, and experimental setup are offered in Sec.D.1, D.2, D.3 respectively.

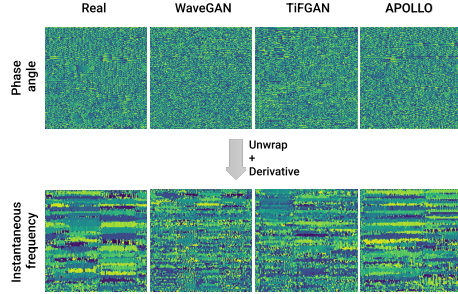
Table 1: Comparison with adversarial methods on unconditional generation. Higher IS (lower FID, NDB, JSD) indicates better performance. The symbol '# par' abbreviates the number of parameters (in millions). APOLLO improves upon all the baselines in all metrics. Moreover, APOLLO-Small achieves similar performance with the baselines while reducing parameters by more than 87%.

Unconditional audio generation on SC09 dataset					
Model	IS (\uparrow)	FID (\downarrow)	NDB (\downarrow)	JSD (\downarrow)	# par (M)
Real data	8.01	0.50	0.00	0.011	—
WaveGAN [11]	4.67	41.60	16.00	0.094	36.5
SpecGAN [11]	6.03	—	—	—	36.5
TiFGAN [41]	5.97	26.70	6.00	0.051	42.4
Mel-Spec GAN [21]	5.76	—	—	—	—
BigGAN [23]	6.17	24.72	—	—	—
II-Nets [8]	6.59	13.01	4.40	0.048	45.9
APOLLO, Small	6.48	18.90	4.20	0.038	4.6
APOLLO	7.25	8.15	3.20	0.029	64.1

Results: The log spectrums of audios synthesized by our model are presented in Fig.4a. Quantitative evaluations with adversarial-based models on SC09 dataset are reported in Table.1. APOLLO



(a) The log spectrograms of the real samples and generated samples trained by our models on SC09, Piano, and Drum datasets. For each image, the horizontal (vertical) axis is along the time (frequency). The frequency increases with interval scale from 0 HZ (top) to 8000 HZ (bottom).



(b) The phase information of STFT of the generated samples from different models trained on Piano dataset. Since it is hard to distinguish and compare with the phase angle, we unwrap the angle over the 2π and take its derivative to obtain the instantaneous frequency. Notice that WaveGAN fails to generate realistic instantaneous frequency in most of frequency bins. The instantaneous frequency generated by our model is most consistent with the real one in terms of sharpness.

Figure 4: This figure shows the the representation of the generated audios in the frequency domain.

Table 2: Quantitative evaluation on Piano dataset. APOLLO outperforms the compared baselines by a large margin while the small APOLLO has 69% fewer parameters than WaveGAN.

Model	NDB (\downarrow)	JSD (\downarrow)	# par (M)
Real data	0.00	0.008	—
WaveGAN	24.00	0.547	36.5
TiFGAN	17.60	0.332	42.4
APOLLO, Small	13.20	0.270	11.3
APOLLO	8.80	0.157	42.7

Table 3: Quantitative Evaluation on conditional audio generation on SC09 dataset. APOLLO improves upon BigGAN and Mel-Spec GAN by a considerable margin.

Model	IS (\uparrow)	FID (\downarrow)	# par (M)
Real data	8.01	0.50	—
BigGAN	7.33	24.40	—
Mel-Spec GAN	7.64	—	—
APOLLO	7.73	6.31	61.7

obtains a large improvement upon all the baselines in Inception Score (IS) [56], Frechet Inception Distance (FID) [26], Number of Statistically-Different Bins (NDB), and Jensen-Shannon Divergence (JSD) [53]. The corresponding ‘Small’ model performs similarly to the compared baselines while reducing parameters by more than 87%. Quantitative evaluations on Piano dataset are summarized in Table.2, where we observe that APOLLO improves upon the baselines in NDB and JSD while reducing parameters by more than 69%. Furthermore, we are interested in investigating whether APOLLO could capture the phase information without explicitly modeling the phase in GANs or utilizing additional phase reconstruction technique. To this end, the phase angle and instantaneous frequency produced by different models trained on Piano dataset are visually depicted in Fig.4b. We observe that WaveGAN fails to generate realistic instantaneous frequency in most of frequency bins. The instantaneous frequency generated by our model is the most consistent with the real one in terms of sharpness, which demonstrates that APOLLO could better capture the phase information.

4.1.2 Conditional audio generation

In this section, we examine the proposed APOLLO in conditional audio generation. Further details on the experimental setup are deferred to Sec.D.4. Regarding the dataset: (a) We first study the SC09 dataset, which has been used in the task of unconditional generation. The label is the class of digits. (b) We also investigate a large music dataset, called NSynth, that consists 300,000 musical notes labelled with pitch, instrument, acoustic qualities, and velocity [12]. Each sample lasts for 4 seconds. We use the same subset and the same test/train split as in Engel et al. [13]. The labels are the pitches ranging from MIDI 24 (~ 32 Hz) to MIDI 84 (~ 1000 Hz).

Result: (a) The results in Table.3 demonstrate the improvement over conditional BigGAN [23] and conditional Mel-Spec GAN [21] on SC09 dataset. The visualization of the generated samples and the interpolation experiment are presented in Sec.D.4 and Sec.E.5 respectively. (b) The result on Nsynth dataset are presented in Table.4. APOLLO improves upon GANSynth [13] in terms of FID, NDB, JSD, the required samples for training, while having significantly less parameters.

Table 4: Quantitative evaluation on conditional audio generation. ‘#sam’ abbreviates the total number of samples used during training (in millions). APOLLO improves upon GANSynth in terms of FID, NDB, and JSD. It is rather remarkable that GANSynth is trained with a batch size of 8 with 11 millions samples as reported in Engel et al. [13] while APOLLO is trained with the same batch size with only 0.48 millions samples. Furthermore, APOLLO has 24% fewer parameters than GANSynth.

Conditional audio generation on Nsynth dataset					
Model	FID(↓)	NDB (↓)	JSD (↓)	#sam (M)	# par (M)
Real data	1.44	0.00	0.002	—	—
GANSynth	3.91	30.20	0.362	11.00	14.1
APOLLO	1.98	27.40	0.298	0.48	10.6

4.2 Comparison against non-adversarial models

Previously, we have shown the comparison between our APOLLO and other adversarial-based models with TF representation and have exhibited the excellent performance of APOLLO. As a compensation, in this section, we compare APOLLO with non-adversarial models using waveform representation, e.g., SampleRNN [42], WaveNet [45], DiffWave [37], SASHIMI [16]. This experiment of unconditional generation is conducted on SC09 dataset. The dataset splitting and the details on evaluation metrics e.g., Modified Inception Score [22], AM Score [74], Inception Score (IS) [56], Fréchet Inception Distance (FID) [26] are the same as in Goel et al. [16]. We provide the results in Table.5, which shows that APOLLO outperforms the baselines by a large margin.

Table 5: Comparison with non-adversarial methods. Higher IS, MIS (lower FID, AM) indicate better performance. APOLLO largely improves upon the baselines. As a remark, previous experiment on SC09 use the same protocol as in Donahue et al. [11] while in this experiment, the dataset splitting and the details on evaluation metrics are the same as in Goel et al. [16].

Unconditional audio generation on SC09 dataset					
Model	IS (↑)	FID (↓)	MIS (↑)	AM (↓)	# par (M)
Real data	8.33	0.02	257.6	0.19	—
SampleRNN [42]	1.71	8.96	3.02	1.76	35.0
WaveNet [45]	2.27	5.08	5.80	1.47	4.2
DiffWave [37]	5.26	1.92	51.21	0.68	24.1
SASHIMI [16]	5.94	1.42	69.17	0.59	23.0
APOLLO, Small	6.03	0.69	77.05	0.53	4.6
APOLLO	6.43	0.45	105.82	0.45	64.1

4.3 Multimodal generation: Image-to-speech

In this section, we access APOLLO in multimodal generation in an image to audio experiment. In the experiment, a low-degree APOLLO is used for the complex-valued random noise. Since the pixels of image are real-valued, the corresponding low-degree polynomial is trivially chosen as models with real-valued coefficients. Finally, a high-degree conditional APOLLO with two input variables is chosen to capture the correlations and generate the STFT of the audio. We select SC09 as a source of digit audios and MNIST dataset [38] as a source of digit images. For each audio clip in the training set (18620 audio clips) of SC09, we align 2 images with the same digit from the training set (55000 images) of MNIST without replacement. In total, we create 18620×2 audio-image pairs as the training set. We sample images from the testing set of MNIST to evaluate the model. The metrics reported in Table.6 is calculated by the same pretrained classifier used in Table.1. Further details on the experimental setup are deferred to Sec.D.5.

Results: The results in Table.6 indicate that the best model achieves 72% accuracy. This experiment is more challenging than the corresponding class-conditional generation, owing to the different modality of the input-output pair, instead of the clean one-hot labels provided in the class-conditional generation. That explains the decrease in the score.

Table 6: Quantitative evaluation on Image-to-speech generation on MNIST-SC09 dataset. ‘#acc’ abbreviates the categorial accuracy of the digit of the generated audio.

Image-to-speech generation on MNIST-SC09 dataset				
Model	IS (\uparrow)	FID (\downarrow)	#acc (\uparrow)	# par (M)
Real data	8.01	0.50	0.93	
APOLLO, Small	5.75	26.5	0.68	3.5
APOLLO	6.90	9.58	0.72	46.1

4.4 Further analysis

We conduct further studies and comparisons on models trained on SC09 for unconditional generation.

Inference speed. From Table12, we observe that WaveGAN has the highest inference speed since it synthesizes the audio directly in the time domain. Even though APOLLO can directly output the STFT without phase reconstruction, APOLLO has an augmented inference time due to the complex operations, e.g., complex multiplication. The comparison with II-Nets confirms our hypothesis, since they have a similar number of parameters but operate on the real field and they are faster than the corresponding APOLLO. Nevertheless, when compared with models proposed specifically for audio generation, APOLLO is still faster than TiFGAN, which requires phase reconstruction. A future step for our model would be to further accelerate the complex multiplications, e.g., by implementing them directly in BLAS, instead of the high-level python operations. On the other hand, non-adversarial models, e.g., DiffWave, result in the slowest inference speed due to the reverse process.

Human study. We invite 25 volunteers to assign an ordinal-scale score (1 to 5) to each audio clip based on the sound quality and perception. The qualitative results are summarized in Sec.F.2. Our model obtains the highest Mean Opinion Score (MOS) [52] with respect to the prior art.

Ablation study. A thorough self-evaluation, e.g. interpolation of the inputs or empirical comparison of between different derivations, is deferred to Sec. E (Appendix) due to the constrained space.

4.5 Beyond audio generation

Apart from audio generation, our model can also be adapted in other audio-related tasks. In the experiment of speech enhancement on VoiceBank-DEMAND dataset [61, 67], we demonstrate the advantage of APOLLO over complex-valued neural networks and real-valued neural networks. In additional, we conduct experiment on speech recognition with Speech Commands dataset [70] and showcase the performance of our APOLLO. Details can be found in Sec.F.3 of the appendix.

5 Conclusion

In this work, we propose APOLLO, a high degree complex-valued polynomial expansion for audio-related tasks. The parameters of the polynomial expansion are naturally expressed as high-order tensors, and we utilize standard tensor decompositions to reduce the parameters and implement the expansion with standard ML frameworks. Using different tensor decompositions results in diverse architectures with simple recursive formulations. The interested practitioner can easily derive custom architectures using complex-valued polynomial expansions by changing the factorizations behind the tensor decomposition as we illustrate. To validate the architectures, we conduct a thorough experimental validation in adversarial audio generation. APOLLO outperforms all the prior art by a large margin demonstrating the expressivity of the proposed complex-valued polynomial expansions. We believe this class of functions will be beneficial for synthesizing long audio tracks in the future. Furthermore, our experiments on conditional generation highlight the efficacy of APOLLO on multimodal generation, where the extension to large-scale models, e.g., realistic text-to-speech translation, can be an interesting application for future work.

Acknowledgements

This project has received funding from the European Research Council (ERC) under the European Union’s Horizon 2020 research and innovation programme (grant agreement number 725594 - time-data). This project was partly supported by Zeiss. This work was supported by the Swiss National Science Foundation (SNSF) under grant number 200021_205011.

References

- [1] Martín Arjovsky, Amar Shah, and Yoshua Bengio. Unitary evolution recurrent neural networks. In *International Conference on Machine Learning (ICML)*, 2016.
- [2] Joshua Bassey, Lijun Qian, and Xianfang Li. A survey of complex-valued neural networks. *arXiv preprint arXiv:2101.12249*, 2021.
- [3] Andrew Brock, Jeff Donahue, and Karen Simonyan. Large scale GAN training for high fidelity natural image synthesis. In *International Conference on Learning Representations (ICLR)*, 2019.
- [4] Hyeong-Seok Choi, Jang-Hyun Kim, Jaesung Huh, Adrian Kim, Jung-Woo Ha, and Kyogu Lee. Phase-aware speech enhancement with deep complex u-net. In *International Conference on Learning Representations (ICLR)*, 2019.
- [5] Hyeong-Seok Choi, Janghyun Kim, Jaesung Huh, Adrian Kim, Jung-Woo Ha, and Kyogu Lee. Phase-aware speech enhancement with deep complex u-net. In *International Conference on Learning Representations (ICLR)*, 2019.
- [6] Grigorios Chrysos, Stylianos Moschoglou, Yannis Panagakis, and Stefanos Zafeiriou. Polygan: High-order polynomial generators. *arXiv preprint arXiv:1908.06571*, 2019.
- [7] Grigorios Chrysos, Markos Georgopoulos, and Yannis Panagakis. Conditional generation using polynomial expansions. In *Advances in neural information processing systems (NeurIPS)*, 2021.
- [8] Grigorios G. Chrysos, Stylianos Moschoglou, Giorgos Bouritsas, Yannis Panagakis, Jiankang Deng, and Stefanos Zafeiriou. P-nets: Deep polynomial neural networks. In *Conference on Computer Vision and Pattern Recognition (CVPR)*, 2020.
- [9] Grigorios G. Chrysos, Stylianos Moschoglou, Giorgos Bouritsas, Jiankang Deng, Yannis Panagakis, and Stefanos P Zafeiriou. Deep polynomial neural networks. *IEEE Transactions on Pattern Analysis and Machine Intelligence (T-PAMI)*, 2021.
- [10] Dieleman, Sander and Schrauwen, Benjamin. End-to-end learning for music audio. In *International Conference on Acoustics, Speech and Signal Processing, (ICASSP)*, 2014.
- [11] Chris Donahue, Julian J. McAuley, and Miller S. Puckette. Adversarial audio synthesis. In *International Conference on Learning Representations (ICLR)*, 2019.
- [12] Jesse Engel, Cinjon Resnick, Adam Roberts, Sander Dieleman, Douglas Eck, Karen Simonyan, and Mohammad Norouzi. Neural audio synthesis of musical notes with wavenet autoencoders, 2017.
- [13] Jesse H. Engel, Kumar Krishna Agrawal, Shuo Chen, Ishaan Gulrajani, Chris Donahue, and Adam Roberts. GANSynth: Adversarial neural audio synthesis. In *International Conference on Learning Representations (ICLR)*, 2019.
- [14] Feng-Lei Fan, Mengzhou Li, Fei Wang, Rongjie Lai, and Ge Wang. Expressivity and trainability of quadratic networks. *arXiv preprint arXiv:2110.06081*, 2021.
- [15] C Lee Giles and Tom Maxwell. Learning, invariance, and generalization in high-order neural networks. *Applied optics*, 1987.
- [16] Karan Goel, Albert Gu, Chris Donahue, and Christopher Ré. It’s raw! audio generation with state-space models. *arXiv preprint arXiv:2202.09729*, 2022.

- [17] Ian Goodfellow, Jean Pouget-Abadie, Mehdi Mirza, Bing Xu, David Warde-Farley, Sherjil Ozair, Aaron Courville, and Yoshua Bengio. Generative adversarial nets. In *Advances in neural information processing systems (NeurIPS)*, 2014.
- [18] Daniel Griffin and Jae Lim. Signal estimation from modified short-time fourier transform. *IEEE Transactions on Acoustics, Speech, and Signal Processing*, 1984.
- [19] Albert Gu, Karan Goel, and Christopher Re. Efficiently modeling long sequences with structured state spaces. In *International Conference on Learning Representations (ICLR)*, 2022.
- [20] Ishaan Gulrajani, Faruk Ahmed, Martín Arjovsky, Vincent Dumoulin, and Aaron C. Courville. Improved training of wasserstein gans. In *Advances in neural information processing systems (NeurIPS)*, 2017.
- [21] Dineshraj Gunasekaran, Gautham Venkatraj, Eoin Brophy, and Tomas E. Ward. Improved speech synthesis using generative adversarial networks. In *AICS*, 2020.
- [22] Swaminathan Gurusurthy, Ravi Kiran Sarvadevabhatla, and R Venkatesh Babu. Deligan: Generative adversarial networks for diverse and limited data. In *Conference on Computer Vision and Pattern Recognition (CVPR)*, pages 166–174, 2017.
- [23] Kazi Nazmul Haque, Rajib Rana, John HL Hansen, and Björn Schuller. Guided generative adversarial neural network for representation learning and high fidelity audio generation using fewer labelled audio data. *arXiv preprint arXiv:2003.02836*, 2020.
- [24] David R. Hardoon, Sandor R. Szedmak, and John R. Shawe-taylor. Canonical correlation analysis: An overview with application to learning methods. *Neural Computation*, 2004.
- [25] Kaiming He, Xiangyu Zhang, Shaoqing Ren, and Jian Sun. Deep residual learning for image recognition. In *Conference on Computer Vision and Pattern Recognition (CVPR)*, 2016.
- [26] Martin Heusel, Hubert Ramsauer, Thomas Unterthiner, Bernhard Nessler, and Sepp Hochreiter. Gans trained by a two time-scale update rule converge to a local nash equilibrium. In *Advances in neural information processing systems (NeurIPS)*, 2017.
- [27] Akira Hirose and Shotaro Yoshida. Comparison of complex-and real-valued feedforward neural networks in their generalization ability. In *International Conference on Neural Information Processing*, pages 526–531. Springer, 2011.
- [28] Yi Hu and Philippos C Loizou. Evaluation of objective quality measures for speech enhancement. *IEEE Transactions on audio, speech, and language processing*, 16(1):229–238, 2007.
- [29] Phillip Isola, Jun-Yan Zhu, Tinghui Zhou, and Alexei A Efros. Image-to-image translation with conditional adversarial networks. *Conference on Computer Vision and Pattern Recognition (CVPR)*, 2017.
- [30] Alexey Grigorevich Ivakhnenko. Polynomial theory of complex systems. *IEEE transactions on Systems, Man, and Cybernetics*, 1971.
- [31] Siddhant M. Jayakumar, Wojciech M. Czarnecki, Jacob Menick, Jonathan Schwarz, Jack Rae, Simon Osindero, Yee Whye Teh, Tim Harley, and Razvan Pascanu. Multiplicative interactions and where to find them. In *International Conference on Learning Representations (ICLR)*, 2020.
- [32] Nal Kalchbrenner, Erich Elsen, Karen Simonyan, Seb Noury, Norman Casagrande, Edward Lockhart, Florian Stimberg, Aaron van den Oord, Sander Dieleman, and Koray Kavukcuoglu. Efficient neural audio synthesis. In *International Conference on Machine Learning (ICML)*, 2018.
- [33] Tero Karras, Samuli Laine, and Timo Aila. A style-based generator architecture for generative adversarial networks. In *Conference on Computer Vision and Pattern Recognition (CVPR)*, 2019.

- [34] M.S. Kim and C.C. Guest. Modification of backpropagation networks for complex-valued signal processing in frequency domain. In *International Joint Conference on Neural Networks (IJCNN)*, 1990.
- [35] Diederik P. Kingma and Jimmy Ba. Adam: A method for stochastic optimization. In *International Conference on Learning Representations (ICLR)*, 2015.
- [36] Tamara G Kolda and Brett W Bader. Tensor decompositions and applications. *SIAM review*, 2009.
- [37] Zhifeng Kong, Wei Ping, Jiaji Huang, Kexin Zhao, and Bryan Catanzaro. Diffwave: A versatile diffusion model for audio synthesis. In *International Conference on Learning Representations (ICLR)*, 2021.
- [38] Yann LeCun, Corinna Cortes, and CJ Burges. Mnist handwritten digit database. *ATT Labs [Online]*. Available: <http://yann.lecun.com/exdb/mnist>, 2, 2010.
- [39] Chien-Kuo Li. A sigma-pi-sigma neural network (spsnn). *Neural Processing Letters*, 2003.
- [40] Craig Macartney and Tillman Weyde. Improved speech enhancement with the wave-u-net. *arXiv preprint arXiv:1811.11307*, 2018.
- [41] Andrés Marafioti, Nathanaël Perraudin, Nicki Holighaus, and Piotr Majdak. Adversarial generation of time-frequency features with application in audio synthesis. In *International Conference on Machine Learning (ICML)*, 2019.
- [42] Soroush Mehri, Kundan Kumar, Ishaan Gulrajani, Rithesh Kumar, Shubham Jain, Jose Sotelo, Aaron Courville, and Yoshua Bengio. Samplernn: An unconditional end-to-end neural audio generation model. 2017.
- [43] Takeru Miyato and Masanori Koyama. cGANs with projection discriminator. In *International Conference on Learning Representations (ICLR)*, 2018.
- [44] Sung-Kwun Oh, Witold Pedrycz, and Byoung-Jun Park. Polynomial neural networks architecture: analysis and design. *Computers & Electrical Engineering*, 2003.
- [45] Aaron van den Oord, Sander Dieleman, Heiga Zen, Karen Simonyan, Oriol Vinyals, Alex Graves, Nal Kalchbrenner, Andrew Senior, and Koray Kavukcuoglu. Wavenet: A generative model for raw audio. *arXiv preprint arXiv:1609.03499*, 2016.
- [46] Edouard Oyallon and Stéphane Mallat. Deep roto-translation scattering for object classification. In *Conference on Computer Vision and Pattern Recognition (CVPR)*, 2015.
- [47] Kasper Palkama, Lauri Juvela, and Alexander Ilin. Conditional Spoken Digit Generation with StyleGAN. In *Interspeech*, 2020.
- [48] Jordi Pons, Oriol Nieto, Matthew Prockup, Erik M. Schmidt, Andreas F. Ehmann, and Xavier Serra. End-to-end Learning for Music Audio Tagging at Scale. In *Proceedings of the 19th International Society for Music Information Retrieval Conference*, 2018.
- [49] Zdenek Pruša and Peter L Søndergaard. Real-time spectrogram inversion using phase gradient heap integration. In *Proc. Int. Conf. Digital Audio Effects (DAFx-16)*, 2016.
- [50] Maithra Raghu, Justin Gilmer, Jason Yosinski, and Jascha Sohl-Dickstein. Svcca: Singular vector canonical correlation analysis for deep learning dynamics and interpretability. In *Advances in neural information processing systems (NeurIPS)*. 2017.
- [51] David P. Reichert and Thomas Serre. Neuronal synchrony in complex-valued deep networks. In *International Conference on Learning Representations (ICLR)*, 2014.
- [52] Flavio P. Ribeiro, Dinei A. F. Florêncio, Cha Zhang, and Michael L. Seltzer. Crowdmos: An approach for crowdsourcing mean opinion score studies. *International Conference on Acoustics, Speech and Signal Processing, (ICASSP)*, 2011.
- [53] Eitan Richardson and Yair Weiss. On gans and gmms. Curran Associates Inc., 2018.

- [54] Antony W Rix, John G Beerends, Michael P Hollier, and Andries P Hekstra. Perceptual evaluation of speech quality (pesq)-a new method for speech quality assessment of telephone networks and codecs. In *International Conference on Acoustics, Speech and Signal Processing, (ICASSP)*, 2001.
- [55] W. Rudin, W.A. RUDIN, and Tata McGraw-Hill Publishing Company. *Real and Complex Analysis*. McGraw-Hill Education, 1987.
- [56] Tim Salimans, Ian Goodfellow, Wojciech Zaremba, Vicki Cheung, Alec Radford, Xi Chen, and Xi Chen. Improved techniques for training gans. In *Advances in neural information processing systems (NeurIPS)*, 2016.
- [57] Jonathan Shen, Ruoming Pang, Ron J Weiss, Mike Schuster, Navdeep Jaitly, Zongheng Yang, Zhifeng Chen, Yu Zhang, Yuxuan Wang, Rj Skerrv-Ryan, et al. Natural tts synthesis by conditioning wavenet on mel spectrogram predictions. In *International Conference on Acoustics, Speech and Signal Processing, (ICASSP)*, pages 4779–4783. IEEE, 2018.
- [58] Yoan Shin and Joydeep Ghosh. The pi-sigma network: An efficient higher-order neural network for pattern classification and function approximation. In *International Joint Conference on Neural Networks (IJCNN)*, 1991.
- [59] Jiahao Su, Wonmin Byeon, Jean Kossaifi, Furong Huang, Jan Kautz, and Anima Anandkumar. Convolutional tensor-train lstm for spatio-temporal learning. *Advances in neural information processing systems (NeurIPS)*, 33:13714–13726, 2020.
- [60] Christian Szegedy, Wei Liu, Yangqing Jia, Pierre Sermanet, Scott Reed, Dragomir Anguelov, Dumitru Erhan, Vincent Vanhoucke, and Andrew Rabinovich. Going deeper with convolutions. In *Conference on Computer Vision and Pattern Recognition (CVPR)*, 2015.
- [61] Joachim Thiemann, Nobutaka Ito, and Emmanuel Vincent. The diverse environments multi-channel acoustic noise database (demand): A database of multichannel environmental noise recordings. In *Proceedings of Meetings on Acoustics ICA2013*, volume 19, page 035081. Acoustical Society of America, 2013.
- [62] Chiheb Trabelsi, Olexa Bilaniuk, Ying Zhang, Dmitriy Serdyuk, Sandeep Subramanian, Joao Felipe Santos, Soroush Mehri, Negar Rostamzadeh, Yoshua Bengio, and Christopher J Pal. Deep complex networks. In *International Conference on Learning Representations (ICLR)*, 2018.
- [63] Théo Trouillon, Johannes Welbl, Sebastian Riedel, Éric Gaussier, and Guillaume Bouchard. Complex embeddings for simple link prediction. In *International Conference on Machine Learning (ICML)*, 2016.
- [64] Mark Tygert, Joan Bruna, Soumith Chintala, Yann LeCun, Serkan Piantino, and Arthur Szlam. A mathematical motivation for complex-valued convolutional networks. *Neural computation*, 28(5):815–825, 2016.
- [65] Rafael Valle, Kevin J. Shih, Ryan Prenger, and Bryan Catanzaro. Flowtron: an autoregressive flow-based generative network for text-to-speech synthesis. In *International Conference on Learning Representations (ICLR)*, 2021.
- [66] Aäron van den Oord, Sander Dieleman, Heiga Zen, Karen Simonyan, Oriol Vinyals, Alex Graves, Nal Kalchbrenner, Andrew Senior, and Koray Kavukcuoglu. WaveNet: A Generative Model for Raw Audio. In *Proc. 9th ISCA Workshop on Speech Synthesis Workshop (SSW 9)*, 2016.
- [67] Christophe Veaux, Junichi Yamagishi, and Simon King. The voice bank corpus: Design, collection and data analysis of a large regional accent speech database. In *2013 international conference oriental COCOSA held jointly with 2013 conference on Asian spoken language research and evaluation (O-COCOSA/CASLRE)*, pages 1–4. IEEE, 2013.
- [68] Xiaolong Wang, Ross Girshick, Abhinav Gupta, and Kaiming He. Non-local neural networks. In *Conference on Computer Vision and Pattern Recognition (CVPR)*, June 2018.

- [69] Yuxuan Wang, RJ Skerry-Ryan, Daisy Stanton, Yonghui Wu, Ron J Weiss, Navdeep Jaitly, Zongheng Yang, Ying Xiao, Zhifeng Chen, Samy Bengio, et al. Tacotron: Towards end-to-end speech synthesis. *INTERSPEECH*, 2017.
- [70] Pete Warden. Speech commands: A dataset for limited-vocabulary speech recognition. *arXiv preprint arXiv:1804.03209*, 2018.
- [71] Yan Xiong, Wei Wu, Xidai Kang, and Chao Zhang. Training pi-sigma network by online gradient algorithm with penalty for small weight update. *Neural computation*, 2007.
- [72] Muqiao Yang, Martin Q. Ma, Dongyu Li, Yao-Hung Hubert Tsai, and Ruslan Salakhutdinov. Complex transformer: A framework for modeling complex-valued sequence. In *International Conference on Acoustics, Speech and Signal Processing, (ICASSP)*, 2020.
- [73] Shi-Xiong Zhang, Yifan Gong, and Dong Yu. Encrypted speech recognition using deep polynomial networks. *CoRR*, 2019.
- [74] Zhiming Zhou, Han Cai, Shu Rong, Yuxuan Song, Kan Ren, Weinan Zhang, Jun Wang, and Yong Yu. Activation maximization generative adversarial nets. In *International Conference on Learning Representations (ICLR)*, 2018.

Contents in the appendix

The appendix contains further details and derivations of the APOLLO. Specifically, a detailed notation is developed in Sec A. The variants of APOLLO are studied in Sec B.1, B.2. The differences from II-Nets are explored in Sec B.3. In Sec C, the derivations and the proofs in the main body are further elaborated. Regarding experiments, the evaluation metrics of audio generation are presented in Sec D.2. Further details of the experimental setup on unconditional audio generation, conditional audio generation, and multimodal generation are developed in Sec D.3, D.4, D.5, respectively. Ablation studies on our models are included in Sec E. Additional analyses for the inference speed and human study are discussed in Sec F.1, F.2. Experiments on speech recognition and speech enhancement are included in Sec F.3. Lastly, the societal impact is described in Sec G.

A Detailed notation

Symbols of variables: As a reminder, real-valued matrices (vectors) are symbolized by uppercase (lowercase) boldface letters, e.g., \mathbf{Y} , \mathbf{y} . Tensors are the multidimensional equivalent of matrices. Real-valued tensors are symbolized by calligraphic letters, e.g., \mathcal{Y} . All complex-valued variables are symbolized with wide tilde, e.g., $\tilde{\mathbf{y}}$, $\tilde{\mathbf{Y}}$, $\tilde{\mathcal{Y}}$. The real part (the imaginary part) of a complex-valued variable is accessed by \Re (\Im).

Complex-valued transpose: In this paper, all transposes for complex-valued matrices are trivial transposes (the same as in real-valued field) without calculating complex conjugate.

Matrix products: The *Khatri-Rao* product of two matrices $\tilde{\mathbf{A}} \in \mathbb{C}^{I \times N}$ and $\tilde{\mathbf{C}} \in \mathbb{C}^{J \times N}$ is denoted by $\tilde{\mathbf{A}} \odot \tilde{\mathbf{C}}$. The *Khatri-Rao* product of multiple matrices $\{\tilde{\mathbf{A}}_{[m]} \in \mathbb{C}^{I_m \times N}\}_{m=1}^M$ is denoted by $\tilde{\mathbf{A}}_{[1]} \odot \tilde{\mathbf{A}}_{[2]} \odot \dots \odot \tilde{\mathbf{A}}_{[M]} \doteq \bigodot_{m=1}^M \tilde{\mathbf{A}}_{[m]}$. The *Hadamard* product of $\tilde{\mathbf{A}}, \tilde{\mathbf{C}} \in \mathbb{C}^{I \times N}$ is denoted by $\tilde{\mathbf{A}} * \tilde{\mathbf{C}}$, where the (i, j) element is equal to $a_{(i,j)} b_{(i,j)}$.

Tensors: Consider an M^{th} order tensor: $\tilde{\mathcal{Y}} \in \mathbb{C}^{J_1 \times J_2 \times \dots \times J_{m-1} \times J_m \times J_{m+1} \times \dots \times J_M}$. We address each element by $(\tilde{\mathcal{Y}})_{j_1, j_2, \dots, j_M} \doteq y_{j_1, j_2, \dots, j_M}$. The *mode- m* vector product between the tensor $\tilde{\mathcal{Y}}$ and a vector $\tilde{\mathbf{u}} \in \mathbb{C}^{J_m}$ is denoted by $\tilde{\mathcal{Y}} \times_m \tilde{\mathbf{u}} \in \mathbb{C}^{J_1 \times J_2 \times \dots \times J_{m-1} \times J_{m+1} \times \dots \times J_M}$, yielding an $(M-1)^{\text{th}}$ order tensor:

$$(\tilde{\mathcal{Y}} \times_m \tilde{\mathbf{u}})_{j_1, \dots, j_{m-1}, j_{m+1}, \dots, j_M} = \sum_{j_m=1}^{J_m} \tilde{y}_{j_1, j_2, \dots, j_m} \tilde{u}_{j_m}.$$

The *mode- m* vector product of a complex-valued tensor and multiple complex-valued vectors is denoted as:

$$\tilde{\mathcal{Y}} \times_1 \tilde{\mathbf{u}}^{(1)} \times_2 \tilde{\mathbf{u}}^{(2)} \times_3 \dots \times_M \tilde{\mathbf{u}}^{(M)} = \tilde{\mathcal{Y}} \prod_{m=1}^M \times_m \tilde{\mathbf{u}}^{(m)}.$$

As a generalization of *CANDECOMP/PARAFAC (CP) decomposition* [36] in complex field, complex-valued tensor could be decomposed into a sum of component rank-one tensors. The rank- R CP decomposition of an M^{th} -order tensor $\tilde{\mathcal{Y}}$ is denoted by:

$$\tilde{\mathcal{Y}} \doteq [\tilde{\mathbf{U}}_{[1]}, \tilde{\mathbf{U}}_{[2]}, \dots, \tilde{\mathbf{U}}_{[M]}] = \sum_{r=1}^R \tilde{\mathbf{U}}_r^{(1)} \circ \tilde{\mathbf{U}}_r^{(2)} \circ \dots \circ \tilde{\mathbf{U}}_r^{(M)}, \quad (7)$$

where \circ is the vector outer product. The factor matrices $\{\tilde{\mathbf{U}}_{[m]} = [\tilde{\mathbf{u}}_1^{(m)}, \tilde{\mathbf{u}}_2^{(m)}, \dots, \tilde{\mathbf{u}}_R^{(m)}] \in \mathbb{C}^{I_m \times R}\}_{m=1}^M$ collect the vectors from the rank-one components. Particularly, we can express the CP decomposition in matrix form:

$$\tilde{\mathbf{W}}_{(1)} \doteq \tilde{\mathbf{U}}_{[1]} \left(\bigodot_{m=2}^M \tilde{\mathbf{U}}_{[m]} \right)^T. \quad (8)$$

Lemma A.1. Given the sets of real-valued matrices $\{\mathbf{A}_\nu \in \mathbb{R}^{I_\nu \times K}\}_{\nu=1}^N$ and $\{\mathbf{C}_\nu \in \mathbb{R}^{I_\nu \times L}\}_{\nu=1}^N$, the following equality holds:

$$\left(\bigodot_{\nu=1}^N \mathbf{A}_\nu \right)^T \cdot \left(\bigodot_{\nu=1}^N \mathbf{C}_\nu \right) = (\mathbf{A}_1^T \cdot \mathbf{C}_1) * \dots * (\mathbf{A}_N^T \cdot \mathbf{C}_N). \quad (9)$$

The proof can be found in the appendix of Chrysos et al. [6].

Lemma A.2. *Given the sets of complex-valued matrices $\{\tilde{\mathbf{A}}_\nu \in \mathbb{C}^{I_\nu \times K}\}_{\nu=1}^N$ and $\{\tilde{\mathbf{C}}_\nu \in \mathbb{C}^{I_\nu \times L}\}_{\nu=1}^N$, the following equality holds:*

$$\left(\bigodot_{\nu=1}^N \tilde{\mathbf{A}}_\nu\right)^T \cdot \left(\bigodot_{\nu=1}^N \tilde{\mathbf{C}}_\nu\right) = (\tilde{\mathbf{A}}_1^T \cdot \tilde{\mathbf{C}}_1) * \dots * (\tilde{\mathbf{A}}_N^T \cdot \tilde{\mathbf{C}}_N). \quad (10)$$

The proof is the same as that of Lemma A.1 except the field (\mathbb{R} or \mathbb{C}) of the matrices.

B Model variants

This section introduces different variants of our proposed framework. The dimension and the field (\mathbb{R} or \mathbb{C}) of learnable parameters in all proposed models are summarized in Table 7 and the corresponding schematics are depicted in Fig 5. In the main body, we have already provided three models, below we complement those with the remaining models.

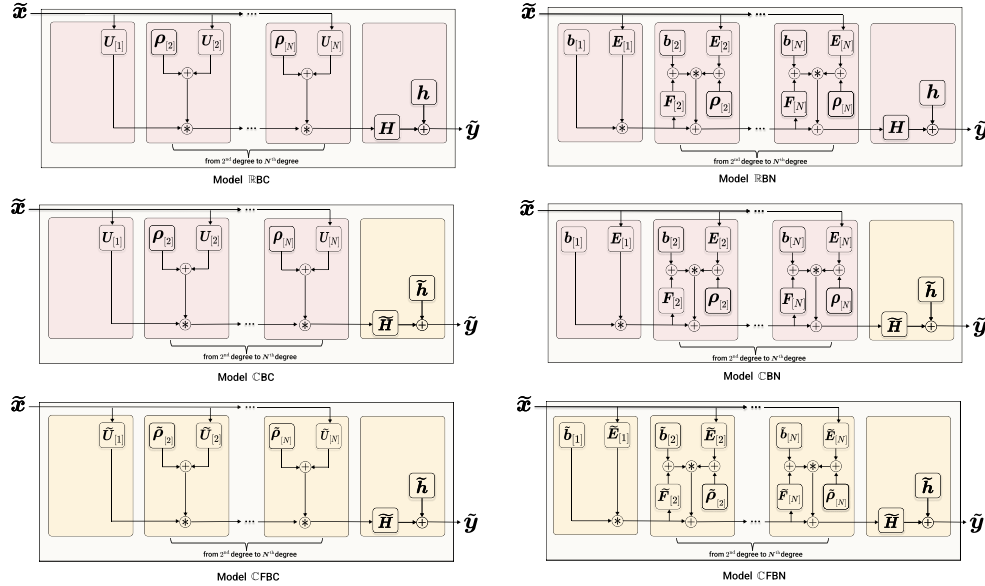


Figure 5: Schematic summary of our proposed models. All learnable parameters inside pink blocks (yellow blocks) are real-valued (complex-valued). We observe that CBC (CBN) reduces the number of parameters of CFBC (CFBN) by changing the field ($\mathbb{C} \rightarrow \mathbb{R}$) of the parameters from 1st degree to N^{th} degree.

Table 7: Table with detailed symbol reference per model.

Symbol	Dimension(s)	Definition
$\mathbf{H}, \mathbf{h}, \mathbf{U}_{[n]}, \rho_{[n]}$	$\mathbb{R}^{o \times k}, \mathbb{R}^o, \mathbb{R}^{d \times k}, \mathbb{R}^k$	Parameters in RBC
$\mathbf{H}, \mathbf{h}, \mathbf{E}_{[n]}, \mathbf{F}_{[n]}, \mathbf{b}_{[n]}, \rho_{[n]}$	$\mathbb{R}^{o \times k}, \mathbb{R}^o, \mathbb{R}^{d \times k}, \mathbb{R}^{k \times k}, \mathbb{R}^k, \mathbb{R}^k$	Parameters in RBN
$\tilde{\mathbf{H}}, \tilde{\mathbf{h}}, \mathbf{U}_{[n]}, \rho_{[n]}$	$\mathbb{C}^{o \times k}, \mathbb{C}^o, \mathbb{R}^{d \times k}, \mathbb{R}^k$	Parameters in CBC
$\tilde{\mathbf{H}}, \tilde{\mathbf{h}}, \mathbf{E}_{[n]}, \mathbf{F}_{[n]}, \mathbf{b}_{[n]}, \rho_{[n]}$	$\mathbb{C}^{o \times k}, \mathbb{C}^o, \mathbb{R}^{d \times k}, \mathbb{R}^{k \times k}, \mathbb{R}^k, \mathbb{R}^k$	Parameters in CBN
$\tilde{\mathbf{H}}, \tilde{\mathbf{h}}, \tilde{\mathbf{U}}_{[n]}, \tilde{\rho}_{[n]}$	$\mathbb{C}^{o \times k}, \mathbb{C}^o, \mathbb{C}^{d \times k}, \mathbb{C}^k$	Parameters in CFBC
$\tilde{\mathbf{H}}, \tilde{\mathbf{h}}, \tilde{\mathbf{E}}_{[n]}, \tilde{\mathbf{F}}_{[n]}, \tilde{\mathbf{b}}_{[n]}, \tilde{\rho}_{[n]}$	$\mathbb{C}^{o \times k}, \mathbb{C}^o, \mathbb{C}^{d \times k}, \mathbb{C}^{k \times k}, \mathbb{C}^k, \mathbb{C}^k$	Parameters in CFBN

B.1 APOLLO with complex-valued coefficients

In the main body, we have introduced fully coupled decomposition with complex-valued coefficients. Below, we provide its corresponding nested coupled decomposition variants.

CBN (Nested decomposition with bias) Unlike CBC, we apply a joint hierarchical decomposition instead of separating the interactions between different degrees. The learnable hyper-parameters $\beta_{[n]} \in \mathbb{R}^\omega$ for $n = 1, \dots, N$, are introduced as scaling factors and (1) becomes:

$$\tilde{\mathbf{y}} = \sum_{n=1}^N \left(\tilde{\mathcal{W}}^{[n]} \times_2 \beta_{[N+1-n]} \prod_{j=3}^{n+2} \times_j \tilde{\mathbf{x}} \right) + \tilde{\mathbf{h}}. \quad (11)$$

The interactions between different degrees are learned through a joint hierarchical decomposition on the polynomial parameters.

- First-degree parameters: $\tilde{\mathcal{W}}_{(1)}^{[1]} = \tilde{\mathbf{H}}(\mathbf{E}_{[3]} \odot \mathbf{B}_{[3]})^T$.
- Second-degree parameters: $\tilde{\mathcal{W}}_{(1)}^{[2]} = \tilde{\mathbf{H}} \left\{ \mathbf{E}_{[3]} \odot \left[(\mathbf{E}_{[2]} \odot \mathbf{B}_{[2]}) \mathbf{F}_{[3]} \right] \right\}^T$.
- Third-degree parameters: $\tilde{\mathcal{W}}_{(1)}^{[3]} = \tilde{\mathbf{H}} \left\{ \mathbf{E}_{[3]} \odot \left[(\mathbf{E}_{[2]} \odot \{ (\mathbf{E}_{[1]} \odot \mathbf{B}_{[1]}) \mathbf{F}_{[2]} \}) \mathbf{F}_{[3]} \right] \right\}^T$,

where $\tilde{\mathbf{H}} \in \mathbb{C}^{o \times k}$, $\mathbf{E}_{[n]} \in \mathbb{R}^{d \times k}$, $\mathbf{B}_{[n]} \in \mathbb{R}^{\omega \times k}$, $\mathbf{F}_{[n]} \in \mathbb{R}^{k \times k}$ for $n = 1, \dots, N$. Similarly, we can obtain the recursive form for N^{th} degree expansion:

$$\tilde{\mathbf{y}}_n = (\mathbf{E}_{[n]}^T \tilde{\mathbf{x}}) * (\mathbf{F}_{[n]}^T \tilde{\mathbf{y}}_{n-1} + \mathbf{b}_{[n]}),$$

for $n = 2, \dots, N$ with $\tilde{\mathbf{y}}_1 = (\mathbf{E}_{[1]}^T \tilde{\mathbf{x}}) * (\mathbf{b}_{[1]})$, $\tilde{\mathbf{y}} = \tilde{\mathbf{H}} \tilde{\mathbf{y}}_N + \tilde{\mathbf{h}}$, where we denote by $\mathbf{b}_{[n]} = \mathbf{B}_{[n]}^T \beta_{[n]}$ for $n = 1, \dots, N$. Motivated by the skip connections in ResNet [25], we embed a shortcut connection into the relationship. In addition, we add a bias term $\rho_{[n]} \in \mathbb{R}^k$, which is similar to CBC. The final recursive relationship:

$$\tilde{\mathbf{y}}_n = (\mathbf{E}_{[n]}^T \tilde{\mathbf{x}} + \rho_{[n]}) * (\mathbf{F}_{[n]}^T \tilde{\mathbf{y}}_{n-1} + \mathbf{b}_{[n]}) + \tilde{\mathbf{y}}_{n-1}, \quad (12)$$

for $n = 2, \dots, N$ with $\tilde{\mathbf{y}}_1 = (\mathbf{E}_{[1]}^T \tilde{\mathbf{x}}) * (\mathbf{b}_{[1]})$ and $\tilde{\mathbf{y}} = \tilde{\mathbf{H}} \tilde{\mathbf{y}}_N + \tilde{\mathbf{h}}$. Note that all learnable parameters in all degrees are real-valued except in the highest degree.

CFBN (Fully nested decomposition with bias) When all the parameters in CBN are complex-valued, we have the following recursive relationship:

$$\tilde{\mathbf{y}}_n = (\tilde{\mathbf{E}}_{[n]}^T \tilde{\mathbf{x}} + \tilde{\rho}_{[n]}) * (\tilde{\mathbf{F}}_{[n]}^T \tilde{\mathbf{y}}_{n-1} + \tilde{\mathbf{b}}_{[n]}) + \tilde{\mathbf{y}}_{n-1}, \quad (13)$$

for $n = 2, \dots, N$ with $\tilde{\mathbf{y}}_1 = (\tilde{\mathbf{E}}_{[1]}^T \tilde{\mathbf{x}}) * (\tilde{\mathbf{b}}_{[1]})$, $\tilde{\mathbf{y}} = \tilde{\mathbf{H}} \tilde{\mathbf{y}}_N + \tilde{\mathbf{h}}$, where we denote by $\tilde{\mathbf{b}}_{[n]} = \tilde{\mathbf{B}}_{[n]}^T \tilde{\beta}_{[n]}$ for $n = 1, \dots, N$.

B.2 APOLLO with real-valued coefficients

The models derived in the main body assume complex-valued coefficients. However we can replace the coefficients in (1) with its real-valued counterpart and obtain the following polynomial:

$$\tilde{\mathbf{Y}} = \sum_{n=1}^N \left(\mathcal{W}^{[n]} \prod_{j=2}^{n+1} \times_j \tilde{\mathbf{x}} \right) + \mathbf{h}, \quad (14)$$

where $\left\{ \mathcal{W}^{[n]} \in \mathbb{R}^{o \times \prod_{m=1}^n \times_m d} \right\}_{n=1}^N$ and $\mathbf{h} \in \mathbb{R}^o$ are learnable parameters. Similarly, we can apply different decomposition techniques to reduce the parameters and obtain the recursive relationship between different degrees. Since the only difference from the models given in the main paper is the field (\mathbb{R} or \mathbb{C}) of the learnable parameters, we skip the derivation and the recursive relationship. If we convert all the parameters in CBC from complex-valued to real-valued, we can obtain RBC. If we convert all the parameters in CBN from complex-valued to real-valued, we can obtain RBN.

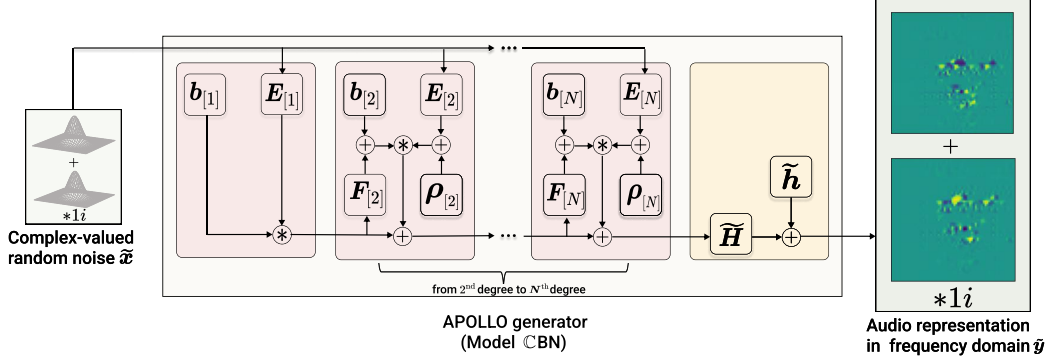


Figure 6: Schematic of the unconditional APOLLO generator, where the complex-valued output is a polynomial of the complex-valued input. The input of the generator is the complex-valued noise and the output is the representation of audio in the frequency domain (e.g., STFT, CQT). All learnable parameters inside the pink blocks (yellow blocks) are real-valued (complex-valued).

B.3 In-depth difference from real-valued polynomial networks

The family of II-Nets bears resemblance with the proposed APOLLO, however those two differ substantially in the following ways:

- The family of II-Nets was designed for real-valued inputs and outputs with all the learnable parameters being real-valued as well. On the contrary, the proposed APOLLO enables using complex-valued inputs or outputs.
- The motivation for designing the two models differs: in APOLLO the goal is to construct an efficient method for time-frequency representations frequently met in audio-related tasks. On the contrary, II-Nets is (mostly) focused on image-related tasks or non-euclidean meshes. In Sec 3.4, we design several architectures and technique to adapt our decomposition to audio generation. As shown in Table 1, our APOLLO greatly outperforms II-Nets, which are trivially adapted to audio generation.
- Beyond the technical tensor decompositions, a significant contribution in our case is to highlight which decompositions work well in the complex field. Even though there are several combinations of recursive formulations that could be designed, we showcase how to construct efficient recursive formulations in a principled way.
- II-Nets express a polynomial expansion of one variable, which presents an issue in case of multiple input variables being available. Particularly, in the case of the variables representing different type of data, e.g., vectors and tensors, it might be more convenient to not concatenate them. This was similarly reported in Chrysos et al. [7], and we follow that model in conditional generation. Concretely, in the image to audio experiment, II-Nets needs to vectorize the input image to concatenate it with the noise, which would destroy the spatial correlations while in APOLLO, we utilize low-degree polynomial to capture the representation and then use a high-degree polynomial to learn the correlation.

C Model derivations

C.1 Derivations for $\mathbb{C}FC$

By leveraging the factorizations, i.e.,

- First degree parameters: $\tilde{\mathbf{W}}^{[1]} = \tilde{\mathbf{H}}\tilde{\mathbf{U}}_{[1]}^T$.
- Second degree parameters: $\tilde{\mathbf{W}}_{(1)}^{[2]} = \tilde{\mathbf{H}}(\tilde{\mathbf{U}}_{[3]} \odot \tilde{\mathbf{U}}_{[1]})^T + \tilde{\mathbf{H}}(\tilde{\mathbf{U}}_{[2]} \odot \tilde{\mathbf{U}}_{[1]})^T$.
- Third degree parameters: $\tilde{\mathbf{W}}_{(1)}^{[3]} = \tilde{\mathbf{H}}(\tilde{\mathbf{U}}_{[3]} \odot \tilde{\mathbf{U}}_{[2]} \odot \tilde{\mathbf{U}}_{[1]})^T$,

the third degree expansion of (1) is expressed as:

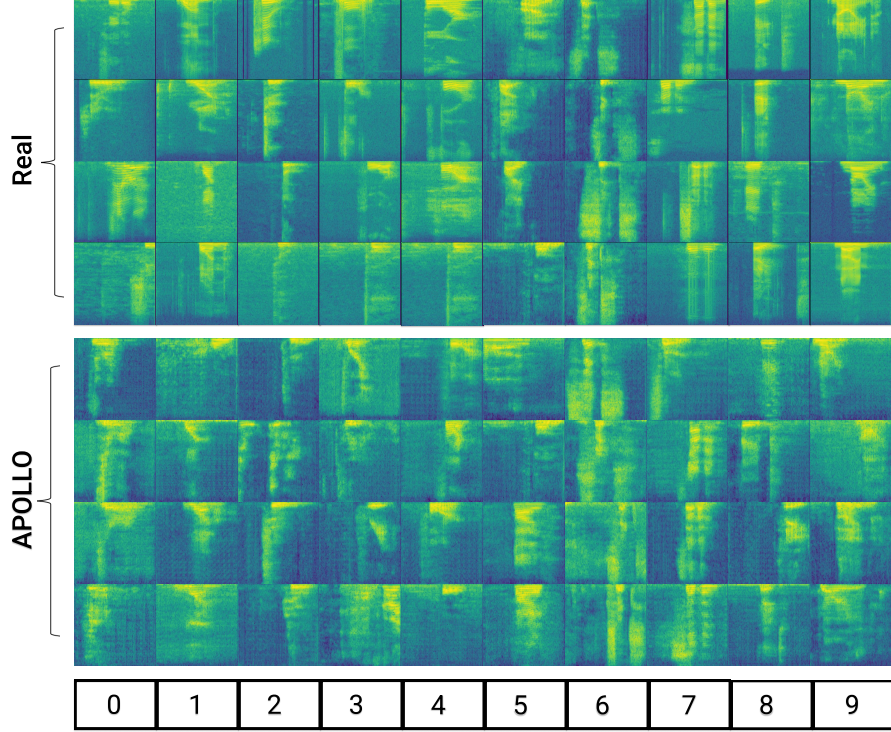


Figure 7: The log spectrum of the real samples and the samples generated by APOLLO trained on SC09 dataset for class-conditional generation. Each column indicates the category from 0 to 9. Our model is able to produce realistic log spectrum in the case of conditional generation.

$$\begin{aligned} \tilde{y} = & \tilde{h} + \tilde{H} \tilde{U}_{[1]}^T \tilde{x} + \tilde{H} \left(\tilde{U}_{[3]} \odot \tilde{U}_{[1]} \right)^T (\tilde{x} \odot \tilde{x}) + \tilde{H} \left(\tilde{U}_{[2]} \odot \tilde{U}_{[1]} \right)^T (\tilde{x} \odot \tilde{x}) \\ & + \tilde{H} \left(\tilde{U}_{[3]} \odot \tilde{U}_{[2]} \odot \tilde{U}_{[1]} \right)^T (\tilde{x} \odot \tilde{x} \odot \tilde{x}). \end{aligned} \quad (15)$$

Applying Lemma A.2 on (15), we obtain:

$$\tilde{y} = \tilde{h} + \tilde{H} \left\{ (\tilde{U}_{[3]}^T \tilde{x}) * \left[(\tilde{U}_{[2]}^T \tilde{x}) * (\tilde{U}_{[1]}^T \tilde{x}) + \tilde{U}_{[1]}^T \tilde{x} \right] + (\tilde{U}_{[2]}^T \tilde{x}) * (\tilde{U}_{[1]}^T \tilde{x}) + \tilde{U}_{[1]}^T \tilde{x} \right\}, \quad (16)$$

which could be expressed as the recursive relationship (2).

C.2 Derivations for CFBC

A polynomial expansion of order $N \in \mathbb{N}$ with output $\tilde{y} \in \mathbb{C}^o$ has the form:

$$\tilde{y} = \sum_{n=1}^N \underbrace{\sum_{r_1=2}^{n+1} \sum_{r_2=r_1+1}^{n+2} \dots \sum_{r_{N-n}=r_{N-n-1}+1}^N}_{(N-n) \text{ sums}} \left(\tilde{\mathcal{W}}^{[n, r_1, r_2, \dots, r_{N-n}]} \prod_{j=2}^{n+1} \times_j \tilde{x} \prod_{\tau=n+2}^{N+1} \times_{\tau} \tilde{\rho}_{[r_{\tau-n-1}]} \right) + \tilde{h}, \quad (17)$$

where we add the scaling parameters $\{\tilde{\rho}_{[n]} \in \mathbb{C}^k\}_{n=1}^N$. Then, the tensors $\{\tilde{\mathcal{W}}^{[n, r_1, r_2, \dots, r_{N-n}]} \}_{n=1}^N$ and $\{\tilde{\rho}_{[n]} \}_{n=1}^N$ are the learnable parameters. Similarly, to previous cases, the learnable parameters are increasing exponentially, so a standard decomposition will be applied to reduce them.

Let us rewrite (17) for a third-degree polynomial, i.e. $N = 3$, to illustrate the decomposition and then we provide the recursive relationship that can be used for an arbitrary degree of expansion. The third degree expansion of (17) has the following form:

$$\begin{aligned} \tilde{\mathbf{y}} = & \widetilde{\mathcal{W}}^{[1,2,3]} \times_2 \tilde{\mathbf{x}} \times_3 \tilde{\boldsymbol{\rho}}_{[2]} \times_4 \tilde{\boldsymbol{\rho}}_{[3]} + \widetilde{\mathcal{W}}^{[2,2]} \times_2 \tilde{\mathbf{x}} \times_3 \tilde{\mathbf{x}} \times_4 \tilde{\boldsymbol{\rho}}_{[2]} + \\ & \widetilde{\mathcal{W}}^{[2,3]} \times_2 \tilde{\mathbf{x}} \times_3 \tilde{\mathbf{x}} \times_4 \tilde{\boldsymbol{\rho}}_{[3]} + \widetilde{\mathcal{W}}^{[3]} \times_2 \tilde{\mathbf{x}} \times_3 \tilde{\mathbf{x}} \times_4 \tilde{\mathbf{x}} + \tilde{\mathbf{h}}. \end{aligned} \quad (18)$$

Then, based on (18), we can apply a tailored coupled CP decomposition with the following form (in matrix form):

- First degree parameters: $\widetilde{\mathcal{W}}_{(1)}^{[1,2,3]} : \widetilde{\mathbf{H}}(\tilde{\mathbf{U}}_{[1]} \odot \mathbf{I} \odot \mathbf{I})^T$.
- Second degree parameters: $\widetilde{\mathcal{W}}_{(1)}^{[2,2]} : \widetilde{\mathbf{H}}(\tilde{\mathbf{U}}_{[1]} \odot \tilde{\mathbf{U}}_{[3]} \odot \mathbf{I})^T$.
- Second degree parameters: $\widetilde{\mathcal{W}}_{(1)}^{[2,3]} : \widetilde{\mathbf{H}}(\tilde{\mathbf{U}}_{[1]} \odot \tilde{\mathbf{U}}_{[2]} \odot \mathbf{I})^T$.
- Third degree parameters: $\widetilde{\mathcal{W}}_{(1)}^{[3]} : \widetilde{\mathbf{H}}(\tilde{\mathbf{U}}_{[1]} \odot \tilde{\mathbf{U}}_{[2]} \odot \tilde{\mathbf{U}}_{[3]})^T$,

where \mathbf{I} denotes the identity matrix, the parameters $\widetilde{\mathbf{H}} \in \mathbb{C}^{o \times k}$, $\tilde{\mathbf{U}}_{[n]} \in \mathbb{C}^{d \times k}$ for $n = 1, 2, 3$ are learnable. By plugging in the aforementioned factorization into (18) and applying Lemma.A.2, we obtain:

$$\tilde{\mathbf{y}} = \widetilde{\mathbf{H}} \left((\tilde{\mathbf{U}}_{[3]}^T \tilde{\mathbf{x}} + \tilde{\boldsymbol{\rho}}_{[3]}) * (\tilde{\mathbf{U}}_{[2]}^T \tilde{\mathbf{x}} + \tilde{\boldsymbol{\rho}}_{[2]}) * (\tilde{\mathbf{U}}_{[1]}^T \tilde{\mathbf{x}}) \right) + \tilde{\mathbf{h}}. \quad (19)$$

We can generalize the equation above to a general recursive formulation, i.e., (3) in the main body.

C.3 Derivations for CBC

Compared to CFBC, the scaling parameters in CBC is real-valued instead of complex-valued, i.e., $\{\boldsymbol{\rho}_{[n]} \in \mathbb{R}^k\}_{n=1}^N$. The third degree expansion has the following form:

$$\begin{aligned} \tilde{\mathbf{y}} = & \widetilde{\mathcal{W}}^{[1,2,3]} \times_2 \tilde{\mathbf{x}} \times_3 \boldsymbol{\rho}_{[2]} \times_4 \boldsymbol{\rho}_{[3]} + \widetilde{\mathcal{W}}^{[2,2]} \times_2 \tilde{\mathbf{x}} \times_3 \tilde{\mathbf{x}} \times_4 \boldsymbol{\rho}_{[2]} + \\ & \widetilde{\mathcal{W}}^{[2,3]} \times_2 \tilde{\mathbf{x}} \times_3 \tilde{\mathbf{x}} \times_4 \boldsymbol{\rho}_{[3]} + \widetilde{\mathcal{W}}^{[3]} \times_2 \tilde{\mathbf{x}} \times_3 \tilde{\mathbf{x}} \times_4 \tilde{\mathbf{x}} + \tilde{\mathbf{h}}. \end{aligned} \quad (20)$$

We apply a tailored coupled CP decomposition with the following form, (note that $\mathbf{U}_{[n]}$ is real-valued):

- First degree parameters: $\widetilde{\mathcal{W}}_{(1)}^{[1,2,3]} : \widetilde{\mathbf{H}}(\mathbf{U}_{[1]} \odot \mathbf{I} \odot \mathbf{I})^T$.
- Second degree parameters: $\widetilde{\mathcal{W}}_{(1)}^{[2,2]} : \widetilde{\mathbf{H}}(\mathbf{U}_{[1]} \odot \mathbf{U}_{[3]} \odot \mathbf{I})^T$.
- Second degree parameters: $\widetilde{\mathcal{W}}_{(1)}^{[2,3]} : \widetilde{\mathbf{H}}(\mathbf{U}_{[1]} \odot \mathbf{U}_{[2]} \odot \mathbf{I})^T$.
- Third degree parameters: $\widetilde{\mathcal{W}}_{(1)}^{[3]} : \widetilde{\mathbf{H}}(\mathbf{U}_{[1]} \odot \mathbf{U}_{[2]} \odot \mathbf{U}_{[3]})^T$,

where \mathbf{I} denotes the identity matrix, the parameters $\widetilde{\mathbf{H}} \in \mathbb{C}^{o \times k}$, $\mathbf{U}_{[n]} \in \mathbb{R}^{d \times k}$ for $n = 1, 2, 3$ are learnable. By plugging in the aforementioned factorization into (20) and applying Lemma.A.2, we obtain:

$$\tilde{\mathbf{y}} = \widetilde{\mathbf{H}} \left((\mathbf{U}_{[3]}^T \tilde{\mathbf{x}} + \boldsymbol{\rho}_{[3]}) * (\mathbf{U}_{[2]}^T \tilde{\mathbf{x}} + \boldsymbol{\rho}_{[2]}) * (\mathbf{U}_{[1]}^T \tilde{\mathbf{x}}) \right) + \tilde{\mathbf{h}}. \quad (21)$$

We can generalize the equation above to a general recursive formulation, i.e., (4) in the main body.

D Experimental details

This section presents the experimental details, including the description of dataset in Sec D.1, the quantitative metrics in Sec D.2, and the experimental setup in Sec D.3, D.4, D.5. We train our model on a single NVIDIA 2080 Ti GPU.

D.1 Datasets

Firstly, we conduct experiments of unconditional generation on three datasets used in Donahue et al. [11]: (a) Speech Commands Zero Through Nine (SC09) [70] that consists of spoken digits “zero” through “nine.” There are 18,620 audio clips in the training set of SC09 and 2552 audio clips in the testing set. The duration of each sample is around 1 second. The total length of the training set is 5.3 hours. (b) Piano, a music dataset that contains 0.3 hours’ Bach compositions. (c) Drum, a music dataset that contains 0.7 hours’ drum samples in the training set. There are 2350 audio clips in the training set and 224 audio clips in the testing set. The duration of each sample is around 1 second. (d) We conduct the experiment of conditional generation on the same aforementioned SC09 dataset. (e) In addition, we also investigate a large music dataset, called NSynth, that consists 300,000 musical notes labelled with pitch, instrument, acoustic qualities, and velocity [12]. Each sample lasts for 4 seconds. We use the same subset and the same test/train split as in Engel et al. [13]. The labels are the pitches ranging from MIDI 24 ($\sim 32\text{Hz}$) to MIDI 84 ($\sim 1000\text{Hz}$). (f) Note that in the paper of SASHIMI, they use a different splitting for SC09 dataset where there are 31,158 audio clips in the training set (8.7 hours in total). Thus, we train our model again in this training set to fairly compare with the baselines, as reported in Table 5.

D.2 Evaluation metrics in audio generation

- **Inception Score (IS).** Firstly introduced by Salimans et al. [56], IS is used to measure the quality and the diversity of the image generated by GAN. The fake samples are fed into a pretrained Inception Network V3 [60] to get the conditional label distribution. The IS is calculated by averaging the KL divergence between the conditional label distribution and its marginal distribution. The audio samples in SC09 dataset are converted to log spectrum representation with 16k sample rate, 8 ms stride, and 64 ms windows size. The frequency bin is further mapped into mel-scale ranging from 40 Hz to 7800 Hz. We use the same evaluation protocol (50k samples) and the same pre-trained classifier from the paper of WaveGAN [11] to calculate the IS for SC09 dataset.
- **Fréchet Inception Distance (FID).** FID [26] characterizes the Fréchet distance of the intermediate layer’s feature from the pretrained Inception Network V3 between the real image and the generated image. For SC09 dataset, the evaluation protocol and the pre-trained classifier are the same as that in IS. For NSynth dataset, the audio is converted to log spectrum representation with 16k sample rate, 16 ms stride, and 128 ms windows size. The frequency bin is further mapped into mel-scale ranging from 0 Hz to 8000 Hz. we train a CNN-based pitch classifier to calculate the score.
- **Number of Statistically-Different Bins (NDB) and Jensen-Shannon Divergence (JSD).** NDB and JSD are proposed by Richardson and Weiss [53] to measure the diversity between the generated samples and the real samples. The audio is converted to STFT and then mel-spectrogram, as illustrated in Fig 8. For SC09 (Piano, Drum, NSynth) dataset, the mel-scale is ranging from 40 Hz to 7800 Hz (0 Hz to 8000 Hz). The mel-spectrograms of the real samples are clustered by K-means into 50 clusters.
- Unless otherwise mentioned, all evaluation metrics in this paper are based on the aforementioned details. However, due to the popularity of audio synthesis, a variety of techniques have been proposed for evaluation. Specifically, in the comparison with non-adversarial methods, as shown in Table 5, the evaluation protocol follows the paper of SASHIMI [16], which was released within the last few months. We use the same pretrained-model, number of samples (2048), and metrics (IS, Modified Inception Score [22], FID, AM Score [74]). **Modified Inception Score (MIS):** MIS considers both intra-class and inter-class sample diversity. **AM Score:** The difference from IS is that AM Score considers the marginal target distribution of the training set.

D.3 Experimental setup in unconditional audio generation

Each audio clip in all datasets is first down-sampled with 16kHz and padded or clipped to the fixed length of 16384. For the SC09 dataset and Drum dataset, we apply STFT with 8 ms stride, 16 ms windows size, and Hann window, which results in the resolution 129×128 (Frequency \times Time). We use a resolution of 128×128 by truncating the Nyquist bin, i.e., bottom row. The APOLLO is

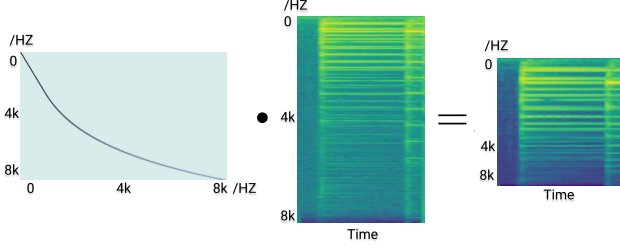


Figure 8: Before calculating JSD, NDB, IS, and FID, we need to project the magnitude of STFT (**Middle**) to human perceptual frequency scales (**Right**) through mel-scale projection matrix (**Left**). The spectrum in the figure are plotted in log-scale only for visualization purpose.

implemented by the product of \mathbb{RBN} and \mathbb{CFBN} . Since the sounds in Piano dataset are not sparse in time domain, we choose 8 ms stride and 32 ms windows. Similarly, we drop the Nyquist bin and get the final solution 256×128 (Frequency \times Time). We choose the product of \mathbb{RBC} and \mathbb{CFBN} . Note that the matrices used to multiply by the noise vector are implemented by dense layer while the matrices used to multiply by the time-frequency representation is implemented by convolution layer. The Hadamard product is implemented by element-wise multiplication. For the hyperparameters, the factor of the gradient penalty is 10. In each step, we apply 5 updates of the discriminator and 1 update of the generator with learning rate 10^{-4} . The hyperparameters of ADAM optimizer [35] are $\beta_1 = 0.5$ and $\beta_2 = 0.9$. The base channel of the CNN is 64 in both generator and discriminator (16 for the 'Small' model). The batch size is 8. The model converges within 380k steps (2 days) in SC09 dataset and 100k steps on Piano dataset and Drum dataset.

D.4 Experimental setup in conditional audio generation

Fig 1 is a schematic illustration of applying (6) on the conditional generator. Motivated by Miyato and Koyama [43], we use a projection discriminator to incorporate the label information. For SC09 dataset, other settings are the same as in unconditional generation. Our model converges within 3 days (450k steps). The log spectrum of the generated samples from 0 to 9 are shown in Fig 7. For NSynth dataset, we choose 16kHz sample rate and pad (or clip) each clip to the fixed length of 64000. Then we apply STFT with 16 ms stride, 128 ms windows size, and 75% overlap, which results in the resolution 1025×128 (Frequency \times Time). After truncating the Nyquist bin, the final resolution is 1024×128 . The APOLLO is implemented by the product of \mathbb{RBN} and \mathbb{CFBN} . The base channel of CNN in our model is 16 in this experiment. Other settings are the same as in conditional generation on SC09. Our model converges within 15 hours (60k Steps).

D.5 Experimental setup in multimodal generation

The architecture of the generator is presented in Fig 3 in the main body, Firstly, we use two low-degree APOLLOs for the random noise and the image. Specifically, we use \mathbb{RBN} for the real-valued image and \mathbb{CFBN} for the complex-valued noise. Then, the conditional APOLLO, i.e., \mathbb{CFBN} , will receive the output of these two low-degree APOLLOs and generate the STFT of the audio. As for the discriminator, we resize the image with nearest-neighbor interpolation to the resolution 128×128 and concatenate it with the STFT of the audio at the input layer. The base channel of CNN is 16 in this experiment. Other settings are the same as in unconditional generation on SC09. Our model converges within one day (200k steps).

E Ablation experiments

E.1 Model variants

We conduct an ablation study on different schemes proposed in this paper. The quantitative results are presented in Table 8, where all models are implemented using products of polynomials, i.e., several polynomials stacked sequentially. ' $\mathbb{RBN} + \mathbb{CFBN}$ ' obtains the best result in IS, NDB, and JSD while ' $\mathbb{RBC} + \mathbb{RBN}$ ' achieves the lowest FID. In practice, the model with full decomposition on complex-

valued coefficients ('CFBN+ CFBN') requires much more parameters, while the improvement is not significant.

Table 8: Ablation experiment on different proposed schemes of APOLLO.

Unconditional audio generation on SC09 dataset					
Model	IS (\uparrow)	FID (\downarrow)	NDB (\downarrow)	JSD (\downarrow)	# par
Real data	8.01 ± 0.24	0.50	0.00 ± 0.00	0.011	—
CBC+CBN	6.74 ± 0.06	9.34	3.80 ± 0.74	0.039	46.0
RBC+CBN	6.98 ± 0.04	12.00	4.00 ± 0.00	0.040	45.9
RBC+RBN	6.79 ± 0.03	8.03	3.80 ± 1.32	0.041	45.9
RBN+RBN	6.71 ± 0.03	9.44	4.00 ± 0.00	0.038	45.9
RBN+CFBN	7.25 ± 0.05	8.15	3.20 ± 1.16	0.029	64.1
CFBN+CFBN	6.84 ± 0.02	8.87	4.20 ± 0.40	0.041	68.1

E.2 The field (\mathbb{C} or \mathbb{R}) of the generator and the discriminator

Below, we conduct experiment with different fields of the generator and discriminator. We combine our APOLLO (RBN+CFBN), with real-valued discriminator and complex-valued discriminator respectively. Additionally, Π -Nets is tested as a real-valued generator that concatenates the real part and the imaginary part of the STFT in two channels. The result in Table 9 illustrates that our model APOLLO with real-valued discriminator yields best IS and FID.

Table 9: Ablation experiment on the field (\mathbb{C} or \mathbb{R}) of generator and discriminator (D). The results demonstrate that combining our complex-valued generator APOLLO with real-valued discriminator yields the best performance in practice.

Unconditional audio generation on SC09 dataset		
Model	IS (\uparrow)	FID (\downarrow)
Real data	8.01 ± 0.24	0.50
Π -Nets-real D	6.59 ± 0.03	13.01
APOLLO-real D	7.25 ± 0.05	8.15
APOLLO-complex D	6.74 ± 0.05	11.76

E.3 Removing activation functions on audio generation

In practice, we add ReLU activations function after all Hadamard products in the implementation, which converts the network into a piece-wise polynomial expansion. In this ablation experiment, we maintain the same setting as in previous experiment except for the generator. Particularly, the generator only contains a hyperbolic tangent in the output space for normalization as typically done in other GAN generators. There is no activation function between the layers. The result in Table 10 shows that both metrics deteriorate without using non-linear activation function. We use the pretrained classifier to calculate the accuracy of the generated samples given the label inputs. Fig 9 shows that the model converges slower and obtains lower accuracy notably after removing non-linear activation functions.

Table 10: Ablation experiment on removing activation function between the layers in the task of conditional generation on SC09. The result shows that our model can be trained without using activation functions (denoted as 'noact'). However, inserting such non-linear operator (denoted as 'act') in each degree significantly boosts the performance in practice.

Conditional audio generation on SC09 dataset		
Model	IS (\uparrow)	FID (\downarrow)
APOLLO-act	7.73 ± 0.04	6.31
APOLLO-noact	6.34 ± 0.03	15.90

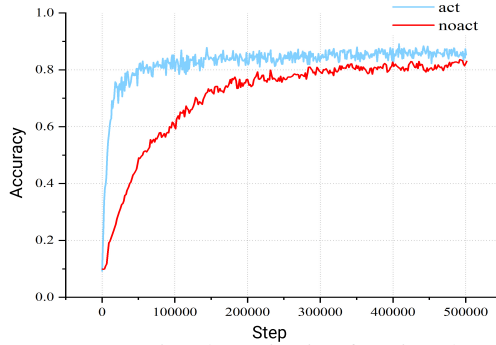


Figure 9: Ablation experiment on removing the activation functions between the layers in the task of conditional audio generation. The figure plots the accuracy of the classes of the generated samples given the label inputs during the training process. The model without activation functions converges more slowly and obtains a lower accuracy.

E.4 Removing activation functions on speech recognition

We have demonstrated the feasibility of removing the activation functions of our model in generative task, in this section, we conduct a similar experiment on audio recognition. That is, we remove the activation functions between the layers. The result in Table 11 shows that our model can obtain similar accuracy even though we remove all the activation functions.

Table 11: Ablation experiment on removing activation function between the layers in the task of speech recognition, the result shows that our model can be trained without using activation functions (denoted as 'noact'). Inserting the non linear ReLU activations function (denoted as 'act') only slightly improves the accuracy.

Classification on Speech Commands Dataset	
Model	Accuracy
APOLLO-act	0.923
APOLLO-noact	0.920

E.5 Qualitative evaluation through interpolation

In this section, we conduct qualitative evaluations of the model through interpolation. We first consider the model of Sec 3.3, i.e., the conditional generation experiment on SC09 dataset. As a reminder, the generator accepts the latent codes, and the class-conditional label (digit).

We fix the class-conditional label, e.g., to digit '9'. We sample two latent codes and we manually annotate the corresponding synthesized audio samples with respect to the gender. We select two latent codes that correspond to a female-attributed voice and a male-attributed voice¹. We then apply a linear interpolation between the two latent codes, which results in ten discrete latent codes. We then use these latent codes and vary the class-conditional label from '0' to '9'. The resulting log spectrum is visualized in Fig 12, where we observe a smooth transition in the log spectrum space. Importantly, the audio samples demonstrate how the voice varies from the beginning of each row (male-attributed voice) to the end of each row (female-attributed voice).

We also conduct the interpolation for the model trained on NSynth dataset. We select two latent codes that correspond to a guitar-attributed audio and a reed-attributed audio. Then we apply the linear interpolation between these two latent codes and vary the pitch from 72 to 24. The resulting log spectrum is visualized in Fig 13, where we observe a smooth transition in the log spectrum space. Notably, as the pitch decreases, the low-frequency component in the log spectrum becomes more prominent.

¹The attribution of gender on the voice is a significant topic that we do not focus on this work; our experiment relies on the annotation of an expert solely for demonstration purpose.

E.6 Similarity of representations between different degrees

To further investigate the properties of the APOLLO, we explore the correlations captured by representations across layers. To that end, we rely on Canonical Correlation Analysis (CCA) [50, 24] to analyze the representations between the different degrees (i.e., layers). Concretely, CCA aims to maximize the correlation between two different sets of variates. In our case, we treat the value after the Hadamard product as the representation of each degree. Since the spatial dimensions of the output of different degrees are not the same, we interpolate the smaller one to match the dimensions. The open-source implementation of singular value CCA [50, 24] is utilized.

As a case study, we use the models of \mathbb{R} BN and CBN that have similar decompositions and differ in the parameters on the last layer. The results are depicted in Fig 10, where we observe that the behavior in different layers of \mathbb{R} BN and CBN is similar. Namely, the representations of different degrees seem to have a localized behavior with the correlations between early-layer representations and last-layer representations to be low.

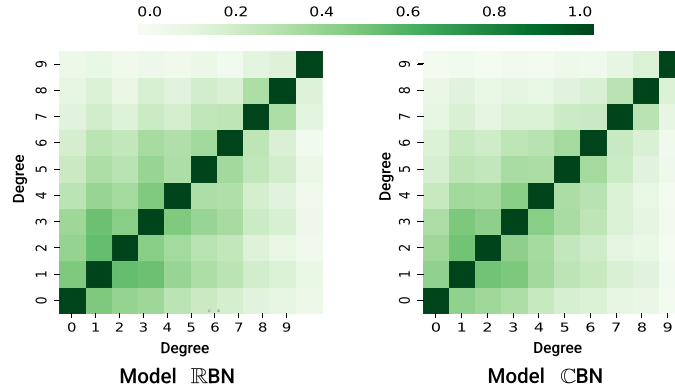


Figure 10: The similarities between the outputs. The color-scale on the top ranges from $[0, 1]$ and dictates the correlation.

F Additional experiments

F.1 Inference speed

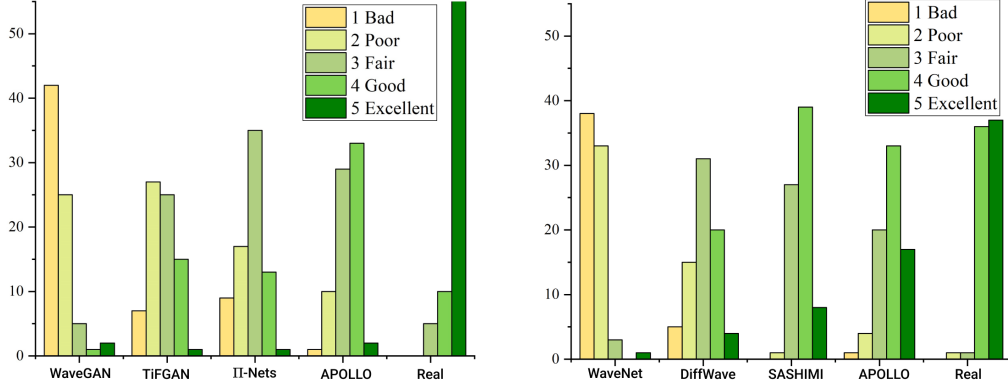
The result is presented in Table 12. WaveGAN has the highest inference speed since it synthesizes the audio directly in the time domain. Notice that the complex operations, e.g., complex multiplication, result in an augmented inference time for the proposed APOLLO. However, the TiFGAN that scored as the top audio model, after our model and the generic Π -Nets, in the human study is more computationally demanding than the proposed model. A future step consists in further improving the small model and making the complex operations more efficient. As for non-adversarial models, we add the comparison with the SOTA model DiffWave and omit SASHIMI, which is implemented by integrating into DiffWave, as mentioned in Goel et al. [16]. We can see DiffWave is the slowest model due to the reverse process.

F.2 Human evaluation

We collect 30 generated samples for each model and 30 real samples. Then we divide these samples into 3 groups and concatenate 10 samples generated by the same model as 1 audio clip which lasts 10 seconds. We invite 25 volunteers whose medium of study are English for the comparison with non-adversarial methods and adversarial methods, respectively. The volunteers are asked to assign an ordinal-scale score (5: excellent, 4: good, 3: fair, 2: poor, 1: bad) to each audio clip based on the sound quality and perceptibility. Finally, we calculate the mean for each model, which is as known as mean opinion score (MOS) [52].

Table 12: This table presents the inference speed for those models unconditionally trained on SC09. ‘#spb’ abbreviates the seconds per batch (batch size = 128) during inference on a single NVIDIA 2080 Ti GPU. ‘# par’ abbreviates the number of parameters.

Model	Frequency domain	Additional phase recovery technique	GAN based	#spb (↓)	# par (↓)
WaveGAN	✗	✗	✓	0.039	36.5
SpecGAN	✓	✓	✓	0.069	36.5
TiFGAN	✓	✓	✓	4.926	43.4
DiffWave	✗	✗	✗	> 480	43.4
II-Nets	✓	✗	✓	0.067	45.9
APOLLO					
RBC+CBN, Small	✓	✗	✓	0.072	3.5
RBC+CBN	✓	✗	✓	0.315	45.9
RBN+CFBN, Small	✓	✗	✓	0.091	4.6
RBN+CFBN	✓	✗	✓	0.374	64.1



(a) This histogram corresponds the experiment in Sec 4.1.1 and shows human evaluation result with our method, adversarial methods, and real data. From left to right, the MOS for all models and real data are 1.61, 2.68, 2.73, 3.33, 4.73, respectively.

(b) This histogram corresponds the experiment in Sec 4.2 and shows human evaluation results with our method, non-adversarial methods, and real data. From left to right, the MOS for all models and real data are 1.57, 3.04, 3.72, 3.81, 4.45, respectively.

Figure 11: Human evaluation on unconditional audio generation on SC09 dataset. The results validate the enhanced performance of APOLLO already indicated by the standard quantitative metrics.

F.3 Beyond audio generation

This section includes additional small-scale experiments on speech recognition and speech enhancement, aiming to show that our networks architecture with the corresponding complex-valued audio representation can also be adapted to other audio-related tasks and achieve considerable performance, which allows future researchers to incorporate our architecture and representations.

F.3.1 Audio classification

We assess the performance in speech recognition on the Speech Commands Dataset [70], which consists of 35 different classes. We choose ResNet [25], its variants Complex ResNet [62], and real-valued polynomial networks(II-Nets) [8] as the baseline. CQT is chosen as the audio representation, where is primitively log-scale along the frequency axis. The inputs of all complex-valued networks are the CQT representation while the inputs of all real-valued networks are the magnitude of the CQT representation. The CQT spans 6 octaves with 32 bins per octave. The sample rate is 16000 and the hop-length is 512. All models are optimized via SGD with momentum 0.9, weight decay 5×10^{-4} . A batch size of 128 is used. The initial learning rate is set to 0.1 and decreased by a factor of 10 at 40, 60, 80, and 100 epochs. Each model is trained for 120 epochs. The channels in each model are [64, 128, 256, 256]. To scrutinize whether our model could still outperform the baselines, we decrease the channels of our model to [64, 96, 128, 256], which is referred to ‘Small’ model. The results are summarized in Table 13. The APOLLO has parameters comparable to the strongest baseline, but

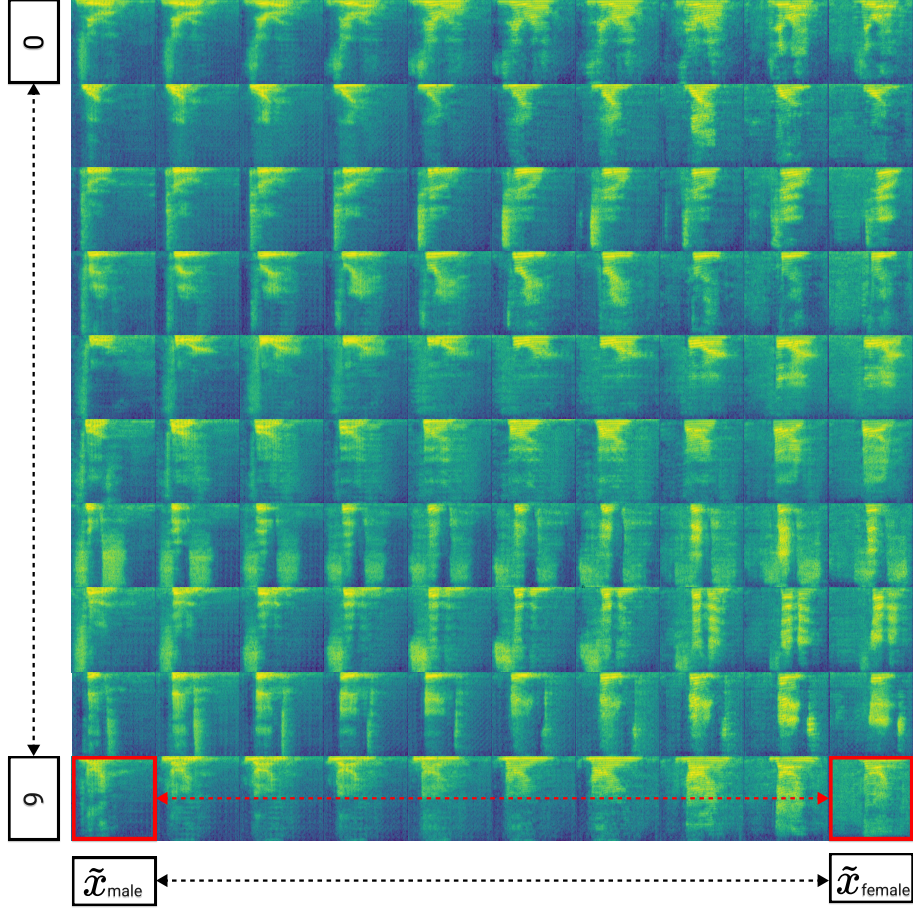


Figure 12: The figure shows the log spectrum of the samples generated by interpolation in the class-conditional model. The full description of the interpolation is on Sec E.5. As a remark, the male (female) attributed voice was annotated by a human expert on synthesized audio samples on digit ‘9’ with random noise \tilde{x}_{male} ($\tilde{x}_{\text{female}}$), i.e., the one demonstrated with red. The rest digits are synthesized by interpolating between the two latent codes along with the digit-based labels, i.e., 0-9 digits.

outperforms all the baselines by a considerable margin. The small APOLLO still outperforms the baseline while reducing the parameters by more than 38%.

Table 13: Speech classification with our model and different ResNet variants on Speech Commands Dataset. Our best model improves the accuracy by 0.6% while the small model still outperforms the baselines with much fewer parameters.

Classification on Speech Commands Dataset with CQT		
Model	Accuracy	#par (M)
ResNet18	0.904	11.8
Complex ResNet18	0.917	10.4
II-Nets ResNet18	0.912	6.0
APOLLO, Small	0.919	3.7
APOLLO	0.923	6.3

F.3.2 Speech enhancement

Next, we conduct a small-scale speech enhancement on VoiceBank-DEMAND dataset [61, 67]. Similar to the previous recognition experiment, we choose baselines that have similar architecture but

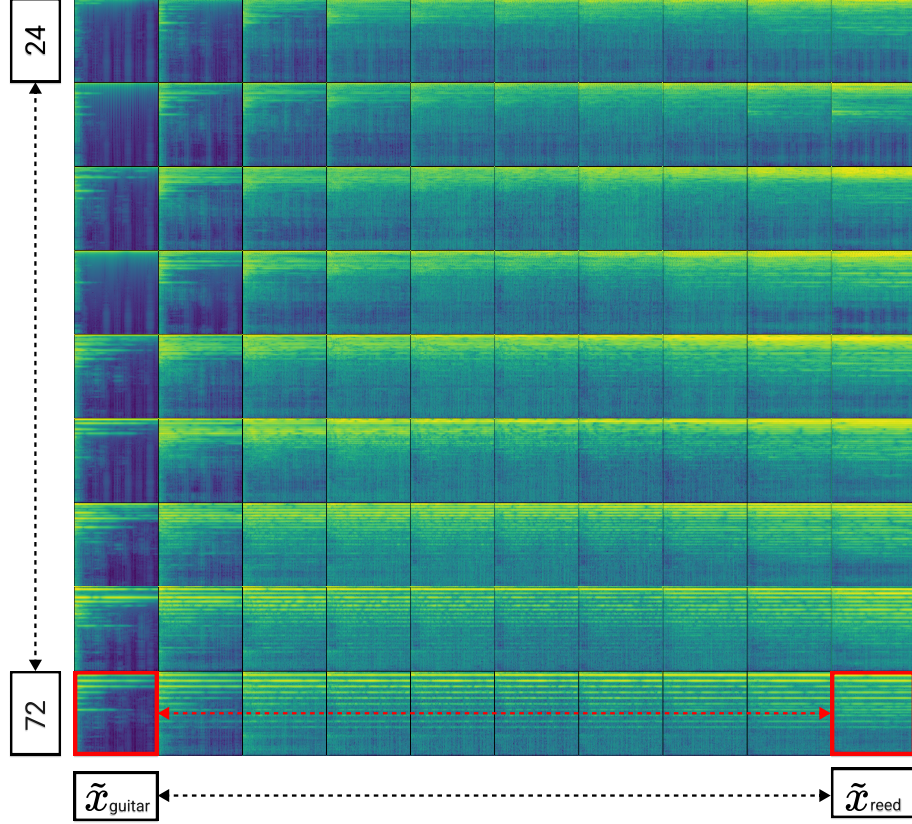


Figure 13: The figure depicts the log spectrum of the samples generated by interpolation in the class-conditional model trained on NSynth dataset. For each small image, the horizontal (vertical) axis is along the time (frequency), the frequency increases with interval scale from top to bottom. The full description of the interpolation is on Sec E.5. As a remark, the guitar (reed) attributed musical instrument sounds was annotated by a human expert on synthesized audio samples on pitch '72' with random noise $\tilde{x}_{\text{guitar}}$ (\tilde{x}_{reed}), i.e., the one demonstrated with red. The rest digits are synthesized by interpolating between the two latent codes along with the pitch-based labels from 24 to 72 with interval scale.

perform in different fields (\mathbb{R} or \mathbb{C}), including (1) Wave-U-Net [40], a real-valued U-Net architecture for the waveform representation. (2) DCUnet [5], a complex-valued U-Net architecture for STFT representation in time-frequency domain. For our model, we convert the decoder of DCUnet to APOLLO. The audios in the training set and testing set are firstly downsampled to 16kHz. We apply STFT with 64ms window size and 16ms hop length. The speech quality is evaluated via perceptual evaluation of speech quality (PESQ) [54] and MOS predictor of signal distortion (CSIG) [28]. Result in Table 14 shows that APOLLO outperforms both baselines, which can be attributed to the expressivity of our complex-valued polynomial networks and corresponding architecture design.

Table 14: Speech classification with our model and different U-net variants. The result demonstrates the increasing performance when using our APOLLO.

Speech enhancement on VoiceBank-DEMAND dataset		
Model	PESQ(\uparrow)	CSIG (\uparrow)
Wave-U-Net	2.40	3.52
DCUnet	3.24	4.34
APOLLO	3.32	4.53

G Societal impact

Our work uses polynomial expansions in the complex fields for audio processing tasks. Among the tasks, we utilize our method for synthesizing audio samples. Audio generation is a significant task with tremendous applications, e.g., human-computer interface. As such, audio generation methods could be used for creating misleading content and we believe that further research is required to ensure the capabilities are used for creating a positive societal impact.

The Generative Adversarial Nets (GANs) [17] that we use for our experiments on audio generation have a dedicated module, i.e., the discriminator, for detecting the real from the fake content. Unfortunately, this is not sufficient for detecting fake content. To that end, we encourage the community to further investigate techniques for discriminating the real from the synthesized audio. Even though our work relies on public benchmarks that are widely used for audio processing, we hope that further research is conducted on how to avoid the negative societal impact from synthesized content.